2015

Radiative Conductivity Analysis Of Low-Density Fibrous Materials

Nima Nouri
University of Kentucky, nima.nouri@uky.edu

STUDENT AGREEMENT:

I represent that my thesis or dissertation and abstract are my original work. Proper attribution has been given to all outside sources. I understand that I am solely responsible for obtaining any needed copyright permissions. I have obtained needed written permission statement(s) from the owner(s) of each third-party copyrighted matter to be included in my work, allowing electronic distribution (if such use is not permitted by the fair use doctrine) which will be submitted to UKnowledge as Additional File.

I hereby grant to The University of Kentucky and its agents the irrevocable, non-exclusive, and royalty-free license to archive and make accessible my work in whole or in part in all forms of media, now or hereafter known. I agree that the document mentioned above may be made available immediately for worldwide access unless an embargo applies.

I retain all other ownership rights to the copyright of my work. I also retain the right to use in future works (such as articles or books) all or part of my work. I understand that I am free to register the copyright to my work.

REVIEW, APPROVAL AND ACCEPTANCE

The document mentioned above has been reviewed and accepted by the student's advisor, on behalf of the advisory committee, and by the Director of Graduate Studies (DGS), on behalf of the program; we verify that this is the final, approved version of the student's thesis including all changes required by the advisory committee. The undersigned agree to abide by the statements above.

Nima Nouri, Student

Dr. Alexandre Martin, Major Professor

Dr. Haluk Karaca, Director of Graduate Studies

RADIATIVE CONDUCTIVITY ANALYSIS OF LOW-DENSITY FIBROUS MATERIALS

DISSERTATION

A dissertation submitted in partial
fulfillment of the requirements for
the degree of Master of Science in
Mechanical Engineering in the
College of Engineering at the
University of Kentucky

By
Nima Nouri
Lexington, Kentucky

Director: Dr. Alexandre Martin, Professor of Mechanical Engineering
Lexington, Kentucky 2015

ABSTRACT OF DISSERTATION

RADIATIVE CONDUCTIVITY ANALYSIS OF LOW-DENSITY FIBROUS MATERIALS

The effective radiative conductivity of fibrous material is an important part of the evaluation of the thermal performance of fibrous insulators. To better evaluate this material property, a three-dimensional direct simulation model which calculates the effective radiative conductivity of fibrous material is proposed. Two different geometries are used in this analysis.

The simplified model assumes that the fibers are in a cylindrical shape and does not require identically-sized fibers or a symmetric configuration. Using a geometry with properties resembling those of a fibrous insulator, a numerical calculation of the geometric configuration factor is carried out. The results show the dependency of thermal conductivity on temperature as well as the orientation of the fibers. The calculated conductivity values are also used in the continuum heat equation, and the results are compared to the ones obtained using the direct simulation approach.

In continue, the simulated model is replaced by a realistic geometry obtained from X-ray micro-tomography. To study the radiative heat transfer mechanism of fibrous carbon, three-dimensional direct simulation modeling is performed. A polygonal mesh computed from tomography is used to study the effect of pore geometry on the overall radiative heat transfer performance of fibrous insulators. An robust procedure is presented for numerical calculation of the geometric configuration factor to study energy-exchange processes among small surface areas of the polygonal mesh. The methodology presented here can be applied to obtain accurate values of the effective conductivity, thereby increasing the fidelity in heat transfer analysis.

This thesis integrates material from one published papers [1] and another one in review. So, some passages have been quoted from these sources.

KEYWORDS: Fibrous geometry, Anisotropic effective conductivity, Radiative heat transfer.

Author's signature: Nima Nouri

Date: September 14, 2015

RADIATIVE CONDUCTIVITY ANALYSIS OF LOW-DENSITY FIBROUS MATERIALS

By
Nima Nouri

Director of Dissertation: Dr. Alexandre Martin

Director of Graduate Studies: Dr. Haluk Karaca

Date: September 14, 2015

Dedicated to my parents Simin and Naser
and my brother Navid

ACKNOWLEDGMENTS

I would like to express my sincere gratitude to my advisor Alexandre Martin, Mechanical Engineering Department at University of Kentucky, for the continuous support of my study and research. His guidance helped me in all the time of research and writing of this thesis.

Besides my advisor, I would like to thank the rest of my thesis committee: Prof. Sean Bailey and Prof. Brad Plaster for their encouragement and insightful comments.

I place on record, my sincere thank you to Brad Plaster, Physics and Astronomy Department at University of Kentucky, for his patience, motivation, enthusiasm and for the continuous support and encouragement regarding the development of this work.

Last but not the least, I would like to thank my parents Simin and Naser, and my brother Navid for supporting me spiritually throughout my life.

TABLE OF CONTENTS

LIST OF FIGURES

LIST OF TABLES

Chapter 1

Introduction

1.1 Background

An object entering a planetary atmosphere (Fig. 1.1) requires a Thermal Protection System (TPS) to shield it from aerodynamic heating. While the re-entering object moves at high speed in atmospheric media, its kinetic energy is mostly dissipated in the form of heat. A fraction of this energy, depending on the surface properties of the materials, is transmitted to its surface by convective and radiative heating. In absence of a proper TPS, the re-entering (spacecraft) object is damaged or even destroyed. The role of the TPS is to block, absorb, or radiate the heat to protect the re-entering object.

A wide range of materials and designs have been studied for space vehicles. The priority in TPS design is to maximize the insulation capability and minimize the vehicle weight to extend the vehicle applicability. Improvements to these materials have been the subject of numerous investigations. Through these studies various types of TPS have been developed: radiative system [3–13], heat-sink system [14,15], transpiration and film cooling system [16–19], ablative system [20], and convective cooling system [21].

Figure 1.1: (color online) An object entering a planetary atmosphere [2].

Each of these systems protects the surface of the space vehicle from heat damage in a different way. Among these thermal protection techniques, the ablative TPS is most widely used because of its satisfactory performance, light weight, relative simplicity, and reliability. The ablative TPS prevents heat penetration into the material by a process called ablation such that the material starts to erode when the surface becomes very hot.

Phenolic Impregnated Carbon Ablator (PICA) is part of a new generation of light-weight fibrous insulators used on re-entry vehicles as thermal protection. [22–30]. It consists of a low density fibrous substrate (FiberForm®, see Fig. 1.2, taken from [31]) impregnated with an organic resin. The arc-jet testing of low density (high porosity) PICA showed [32] that these materials can withstand high heating rates. For such a porous media subjected to high temperature and high temperature gradients, radiative energy exchange within the material becomes important. This radiative heat transfer process can be expressed in the form of a temperature dependent effective

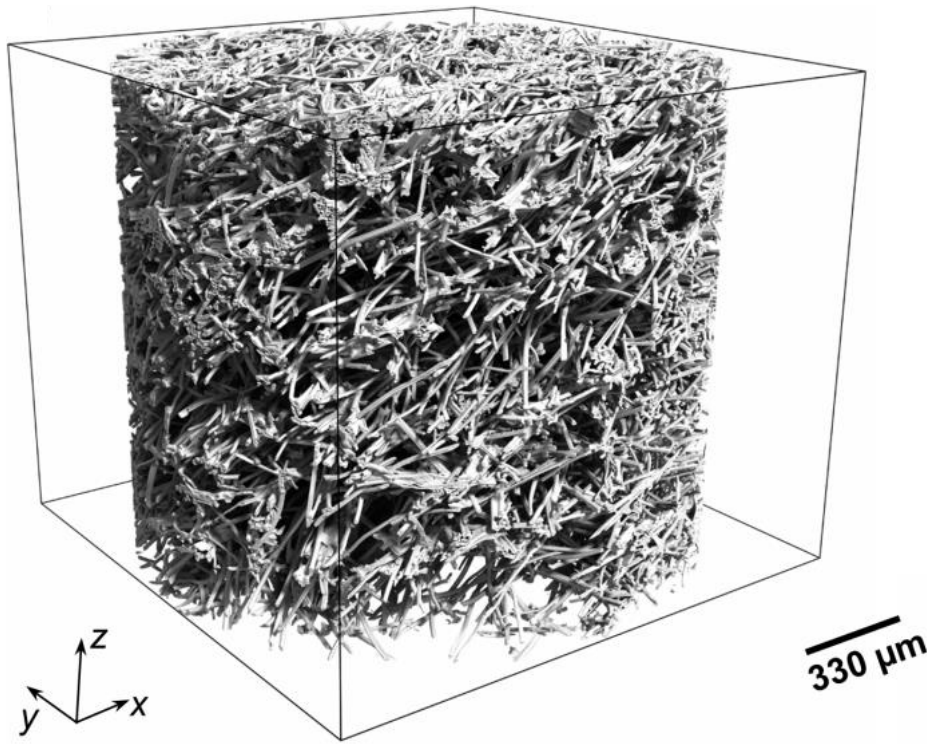

Figure 1.2: (color online) Example of a realistic geometry, obtained using computed micro-tomography (image from [31])

radiative conductivity. Different models are used to study the heat transfer process and, more specifically, the radiative thermal process [33]. These are briefly reviewed in the following section.

1.2 Review of heat transfer models

Heat transfer through fibrous material has been investigated in numerous studies [34–37], and new models have been developed to estimate the porous material response to high-enthalpy environments [38–40]. Briefly, the basic modes of heat transfer in fibrous material are:

1. Gas convection,
2. Gas conduction,
3. Thermal radiation,

4. Fiber-to-fiber conduction.

Gas convection is a very important mechanism in material response, such that the cold gas is transfered into the hot region, and cools the material. In material response modeling, gas convection is no accounted for in the effective heat conductivity, but treated separately in an other term of the governing equations. However, either in case of vacuum (considered in the present study) or if the gas is not moving there is no convection.

Radiation and conduction are other two major processes that must be taken into account in thermal response models. Both of these phenomena require a detailed knowledge of the micro-scale geometry of the material. For radiative transfer, the upscaling task is complex since the process depends on the specific orientation of individual fibers and their geometric configuration factors (GCF); which is the fraction of the radiation which leaves a surface and strikes another surface. The importance of these modes in material response modeling depends on the different values of the porosity and temperature. The relative magnitudes of the different modes of heat transfer in fibrous material have been reported in [41–44]; these are schematically shown in Fig. 1.3. The study of thermal radiation in fibrous material is essential since in high temperature regimes a significant portion of the total heat transfer is composed of thermal radiation. A brief review of various developed analytical and numerical models used in material response studies have been done at [45]. The main goal of these models is an accurate prediction of the radiative properties of the fibrous material.

The importance of the thermal radiation in fibrous insulations under vacuum is experimentally discussed using conducting guarded hot-plate tests in [41]. The guarded hot-plate tests allow the determination of the thermal conductivity of material, if the samples are plane and plate-shaped.

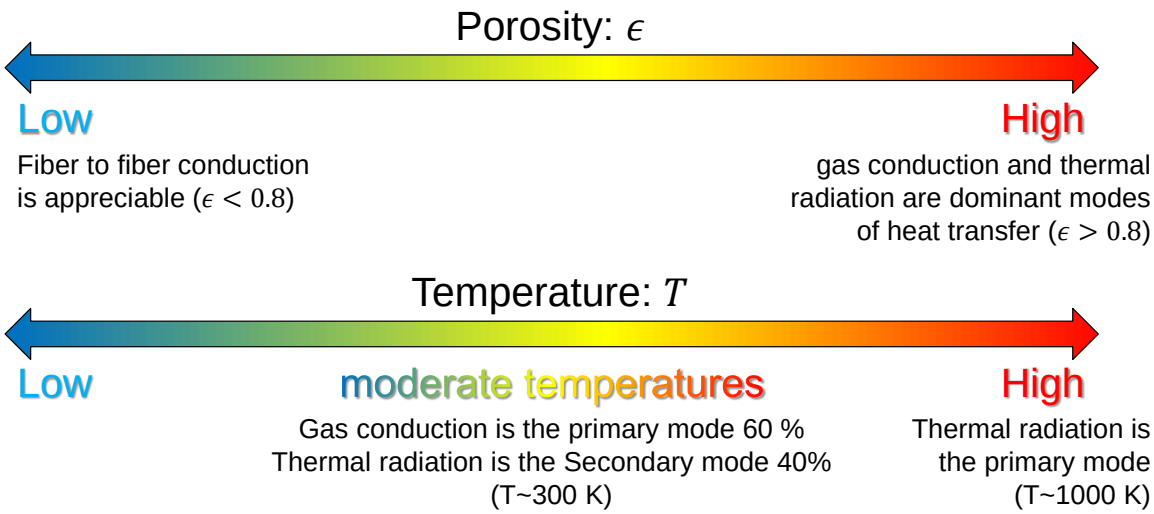

Figure 1.3: (color online) Schematic illustration of the basic modes of heat transfer with respect to the porosity and temperature of the fibrous material.

There are different aspects involved in the thermal radiation studies which need to be addressed:

1. An appropriate transfer model must be developed,

2. The radiative properties must be determined,

3. Effects of the geometry of the fibers should be studied.

Past studies have modeled radiative heat transfer in porous material as a conductive process [46–53]. Simple expressions have been developed for the thermal conductivity due to radiation. Most of these models contain parameters which need to be determined experimentally. A few investigations have been done as well [54–59] to address the problem from a radiative point of view. In follow, we briefly introduce these models.

For a conductive process, from Fourier's law, the radiant flux q [W/m^2] is expressed as

$$q = \kappa_{\text{rad}} \frac{\Delta T}{L}, \tag{1.1}$$

where κ_{rad} [W m^{-1} K^{-1}] is the thermal conductivity due to radiation, ΔT [K] is the absolute temperature difference across the FM, and L [m] is the thickness of the insulation. Thermal radiation diffuses through fibers within an absorbing and emitting regime. The net thermal radiation across the entire material is determined by combining all the contributions from the fibers. The radiative thermal conductivity is then defined by casting the final radiant flux expressions in the form of Eq. 1.1 [53]. It is found that the conductivity due to radiation to be a cubic function of the temperature as T_m^3, where T_m is the mean temperature in the material. It is important to point out that the work presented in this thesis is also in agreement with this cubic dependency on the temperature which is a prediction of Rosseland's hypothesis [61].

Other approaches have been developed based on using a continuous or discontinuous formulation of the Radiative Transfer Equation (RTE). In the first approach [47, 48], the medium is treated as a continuous regime. While, the discontinuous model [49], the system is subdivided into an array of cells of a given geometry. Then, the radiative transfer is calculated in each basic cell by macroscopic methods such as Monte Carlo [50]. However, such models are limited in their applicability and consume much CPU time.

The study done by [54] addressed the problem of the radiation attenuation (gradual loss in intensity of radiation flux through the medium due to absorption and scattering). There, the total radiation through the fibrous material was measured. A two-flux model was used to deduce the absorption and scattering coefficients. The results showed that, in general, the scattering coefficients are orders of magnitude larger than the absorption coefficients. This is in agreement with studies in [60]. The prediction of the coefficients from an analytical approach was also discussed in [54].

In regards to the scattering properties of the porous material, two different criteria of fibers are considered separately:

1. Coarse (non-scattering criteria) where $(2\pi r/\lambda) \gg 1$,

2. Fine (scattering criteria) where $(2\pi r/\lambda) \ll 1$,

where λ denotes the characteristic wavelength of the radiation and r denotes the effective radius of the fibers. An expression for the absorption and scattering coefficients was developed in [55]. The Rayleigh approximation was deployed to estimate the coefficients in the coarse and fine regimes; the size of a scattering particle was parameterized by the ratio $(2\pi r/\lambda)$. The opaque surface assumption was considered [52] for greater simplification; however, this approximation is very restrictive. To prevent the effect of scattering, the diameter of the fibers has to be much larger than the characteristic wavelength of the radiation for the approximation to be valid. Therefore, this model is strictly valid only for fibrous material with large fibers.

The studies which have been done in [56, 57] addressed both radiation and conduction simultaneously in fibrous material. The work done by [56] was based on three different approaches:

1. Radiation transfer equation or its approximations,

2. Approximation of radiation thermal conductivity,

3. Radiation diffusion approximation for radiation transfer.

It was shown that the third approach is the most preferable, since the first and second approaches need experimental measurement of the optical properties. The comparison between the radiation thermal conductivity approximation and the radiation diffusion approximation has been carried out. In [57], a quartic dependence to the temperature (T^4) was approximated by a Taylor series in the differential integral equation governing the temperature distribution which was solved numerically. The heat flux was also numerically determined.

Geometric features of the porous material is another essential parameter, effective on the radiative properties of the material. Different studies have been done to

characterize the effects of the geometry of the fibers using numerical or experimental techniques [62–65].

Regarding the geometrical properties of the fibrous material, a radiation model is developed in [62] to evaluate the effect of the fiber orientation on the radiative heat transfer. The results show that the orientation of the fibers strongly affects both the back-scatter factor and radiative heat transfer.

In order to investigate the effects of the geometrical properties of the fiber preforms, a simplified direct simulation (DS) for a two-dimensional fibrous medium has been proposed by van Eekelen and Lachaud [63]. Based on the hypothesis of Rosseland, they model the thermal radiation process in a fiber preform medium made of randomly positioned, yet parallel and identically-sized, fibers. Although they showed that there is a temperature dependence of the radiative conductivity, the relation to angular dependence was not taken into account.

It has been shown that [66–69] light-weight fibrous insulators such as PICA have a preferred orientation of the fibers and, therefore, show anisotropic behavior. Hence, developing new models with the ability to calculate the material thermal properties using real geometrical features of the fibers is a significant improvement.

More recently, the availability of three-dimensional computed tomography imaging facilitates the studies [64,65]. It is now possible to develop detailed models using the true structure of porous material in digitized form. Also, the effective radiative conductivity due to heat conduction through porous material can be accurately estimated using simple numerical or analytical tools based only upon the information casted from 3D computed tomography. This provides a low-cost alternative compared to using expensive experimental techniques.

The study of the morphology characteristics and ablation behavior of a highly porous carbon fiber perform combining experimental and numerical approaches has been done in [64]. Using the morphological characterization of the 3D structure of

the material, they reported the geometrical properties of the carbon preform such as porosity, specific surface area, and tortuosity. This information then guided them to the study of the diffusion of oxygen through the porous medium by applying a Lagrangian model.

The work which has been done in [65] studied the effective thermal conductivity – a thermal property which combines the contributions of both conduction and radiation – of a porous material (metal foam) at high-temperature regimes using the real geometry obtained from 3D computed tomography. Using the data casted from computed tomography, they numerically predicted the ETC subject to two different 1D models. The first model considered the steady state energy conservation equation for coupled conduction-radiation heat transfer, where the gradient of radiative heat flux is obtained from the solution of coupled conduction-radiation RTE. The second model treats conduction and radiation in a decoupled manner and separately predicts the ETC due to pure radiation using Rosseland approximation. The numerical results casted from these two models have been validated in comparison with panel test experimental techniques.

Various studies have been done for derivation of an analytical expression for the effective thermal conductivity used in TPS of a space vehicle. An analytical expression for determination of the effective thermal conductivity as a function of local conditions is ultimately a suitable tool in computationally intensive large-scale analyses. The results obtained in [70] are shown that such an expression is valid for a large ranges of temperature and pressure. They presented the expression for assessing the performance of a CFOAM-based [71] TPS (a carbon-based foam from high suphur bituminous coal). It is important to note that the work has been done in this thesis, in agreement with Rosseland approximation, is ultimately led to an expression of the effective radiative conductivity as a function of direction and local temperature ($\kappa_{i,j}(T)$, where i and j denote the Cartesian coordinates (x, y, z)) for assessing the

performance of FiberForm®.

Thermal radiation in fibrous material continues to be an active research topic. The development of a proper transfer model and determination of the radiative properties of the fibrous material in accordance with the transfer model are complex and computationally intensive. A bottom line lies on the fact that radiative heat transfer analysis consistently depends upon reliable material property information in addition to accurate radiative transfer modeling techniques. This is despite the fact that the material properties are known to be a source of huge uncertainties.

1.3 Physics of thermal radiation

1.3.1 Thermal radiation

It is critical to understand the underlying physics of thermal radiation. Electromagnetic radiation generated by the thermal motion of charged particles in matter, with a temperature greater than absolute zero, is called thermal radiation. Thermal radiation is a consequence of kinetic energy fluctuations of the atoms or molecules. This then results in charge acceleration and/or dipole oscillation which produces electromagnetic radiation. All matter, even at a single temperature, radiates in a wide spectrum of energies. The types of electromagnetic radiation are broadly classified based on the radiation wavelength, which is a characteristic of the type of radiation. This is listed in Table 1.1.

Thermal radiation can be detected as heat and occurs approximately in the range $0.4 < \lambda < 1000.0$ μm, which includes the visible and the near, middle, and far infrared (IR) regions.

Three physical phenomena contribute to the effective conductivity within porous media: conduction, convection, and radiation. Thermal radiation is different from thermal convection and thermal conduction, such that radiation is able to act at a distance in the absence of an intervening medium, which makes it one of the fun-

Table 1.1: Spectrum of electromagnetic radiation.

Region	Wavelength [cm]	Frequency (G Hz)	Energy(eV)
Radio	> 10	< 3	$< 10^{-5}$
Microwave	$10 - 0.01$	$3 - 3\times10^{3}$	$10^{-5} - 0.01$
Infrared	$0.01 - 7\times10^{-5}$	$3\times10^{3} - 4.3\times10^{5}$	$0.01 - 2$
Visible	$7\times10^{-5} - 4\times10^{-5}$	$4.3\times10^{5} - 7.5\times10^{5}$	$2 - 3$
Ultraviolet	$4\times10^{-5} - 10^{-7}$	$7.5\times10^{5} - 3\times10^{8}$	$3 - 10^{3}$
X-Rays	$10^{-7} - 10^{-9}$	$3\times10^{8} - 3\times10^{10}$	$10^{3} - 10^{5}$
Gamma Rays	$< 10^{-9}$	$> 3\times10^{10}$	$> 10^{5}$

damental mechanisms of heat transfer. Heat transfer by conduction and convection can only occur in the presence of a medium, while for example, thermal radiation emitted by the sun reaches us through empty space. A second distinguishing feature of radiative transfer is that high-temperature radiative energy-exchange becomes important such that the transfer of energy between two bodies depends on the difference between the temperatures of the individual components raised to the fourth power, $\mathcal{O}\left(\Delta(T^4)\right)$. Alternatively, for the material-oriented heat transfer modes (i.e. conduction and convection), this dependency is just on the order of the first power, $\mathcal{O}\left(\Delta(T)\right)$.

1.3.2 Surface radiation properties

Radiation properties of a surface can be listed as:

1. Emissivity ϵ,

2. Absorptivity α,

3. Reflectivity ρ.

The radiation q [W/m^2] that can be emitted from a surface has a quartic dependence (a polynomial function of degree 4) on absolute temperature associated with

the surface. This is governed by the Stefan-Boltzman law,

$$q = \sigma T^4 , \tag{1.2}$$

where σ is the Stefan-Boltzman constant of the value 5.67×10^{-8} [W/(m^2 K^4)]. This is the maximum radiation, called black body radiation, from a surface called a black body. Alternatively, the emitted radiation associated with other surfaces is a fraction of the radiation emitted by a black body at the same temperature which is weighted by emissivity coefficient $0.0 \leq \epsilon \leq 1.0$ and is expressed as

$$q = \epsilon \sigma T^4 . \tag{1.3}$$

Absorptivity α is another important property of a surface which is the fraction of the radiation incident on a surface that is absorbed by the surface. Absorptivity values also range between 0 and 1. The black body absorptivity is equal to 1 which makes it a perfect absorber as well as a perfect emitter. Therefore, a black body in thermal equilibrium, at every frequency, emits as much energy as any other body emits at the same temperature, and emits energy isotropically (i.e. independent of direction).

Finally, reflectivity ρ of a surface is the ratio of reflected power to incident power. All these material characteristics (i.e. ϵ, α, and ρ) are functions of the wavelength (λ) of the electromagnetic radiation, direction (θ and φ), and temperature T (i.e. $\epsilon\,(\lambda, \theta, \varphi, T)$, $\alpha\,(\lambda, \theta, \varphi, T)$ and $\rho\,(\lambda, \theta, \varphi, T)$).

1.3.3 Diffuse-Gray Surface

A common assumption here is that surfaces are *diffuse-gray*. Diffuse signifies that ϵ and α do not depend on direction. The term gray specifies that ϵ and α do not depend on wavelengths. In summary, a diffuse surface has properties independent of direction and a gray surface is characterized by having properties independent of wavelength.

Therefore, a diffuse-gray condition is applied and denotes a surface which absorbs a fixed fraction of incident radiation from any direction and at any wavelength, $\alpha(\lambda, \theta, \varphi, T) = \alpha(T)$. It also denotes a surface which emits radiation that is a fixed fraction of black body radiation for all directions and all wavelengths, $\epsilon(\lambda, \theta, \varphi, T) = \epsilon(T)$.

Furthermore, Kirchhoff's law denotes that – since black body radiation is equal in every direction (isotropic) – the emissivity and the absorptivity, if they happen to be dependent on direction, must be equal for any given direction,

$$\alpha(T) = \epsilon(T). \tag{1.4}$$

1.4 Objective

The study here continues the previous contributions to the analysis, modeling, and understanding of the radiative aspects of the new generation of light-weight insulators used in re-entry vehicles. The objective of this work is to study the high-temperature applications of low-density fibrous material such as FiberForm®. A 3D model is developed, based on FiberForm® micro-structure characteristics, porosity, and surface emissivity values, to quantitatively analyze and determine the radiative properties.

Chapter 2 introduces the concept of the geometric configuration factor which is used in thermal radiation processes. The radiation exchange in an enclosure of diffuse-gray surfaces is also discussed. Chapter 3 and 4 present the new models on the development of a direct simulation of radiative heat transfer processes. An artificial geometry of the cylindrical fibrous material is simulated in chapter 3 to examine the developed model. Then, in chapter 4, the validated model is used on a realistic geometry of FiberForm®. In both cases, the radiative properties are extracted directly from the simulation and no experimentally determined parameters are used. Finally, Chapter 5 gives a brief summary.

Chapter 2

Geometric configuration factor and radiation exchange in an enclosure of diffuse-gray surfaces

2.1 Introduction

The Geometric Configuration Factor calculation is an important aspect in determining the radiation interchange between surface areas. The computation of GCF involves integrating over the solid angles subtended by each surface segment, if surfaces have a common view field. A diffuse-gray surface area radiates across all wavelengths per unit time, due to the temperature of that particular surface, and incident partially on the second surface. The amount of energy exchanged between these two arbitrarly oriented surface areas, A_1 and A_2, is explicitly dependent upon the GCF defined as

$$F_{1\to 2} = \frac{\text{Energy intercepted by } A_2}{\text{Energy leaving } A_1}. \tag{2.1}$$

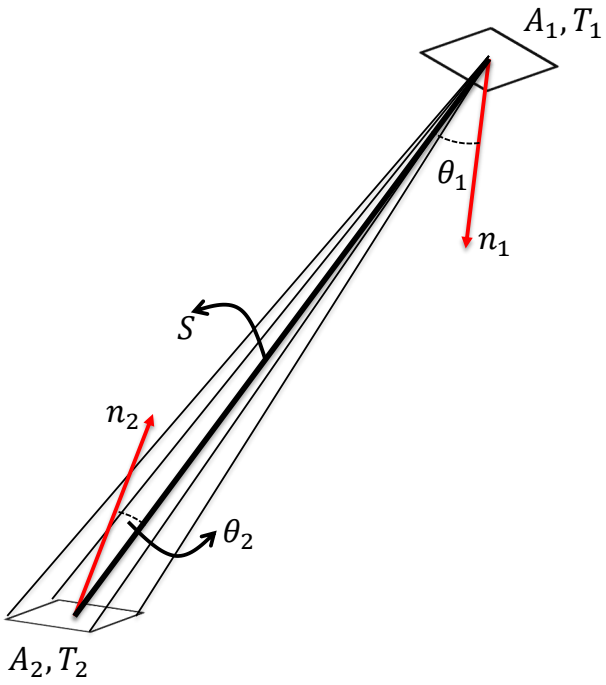

Figure 2.1: (Color online) Schematic configuration of two surface areas arbitrarly oriented in space.

2.2 GCF between two differential elements

The fraction of energy leaving diffuse infinitesimal surface element a_1 that arrives at infinitesimal surface element a_2 is defined as the geometric configuration factor $F_{a_1 \to a_2}$. Let's consider i_1 [W/m^2] as the total intensity leaving a_1. The total energy per unit time [W] leaving a_1 and incident on a_2 can be expressed as

$$W_{a_1 \to a_2} = i_1 \, a_1 \, \cos\theta_1 \, \mathrm{d}\omega_1 \tag{2.2}$$

and vise versa if we consider i_2 as the total intensity leaving a_2; then the total energy per unit time leaving a_2 and incident on a_1 is of the form

$$W_{a_2 \to a_1} = i_2 \, a_2 \, \cos\theta_2 \, \mathrm{d}\omega_2 \, , \tag{2.3}$$

where $d\omega_1$ ($d\omega_2$) is the solid angle subtended by a_2 (a_1) when viewed from $a_1(a_2)$. The differentials $d\omega_1$ and $d\omega_2$ can be written as

$$\begin{aligned} d\omega_1 &= \frac{a_2 \cos\theta_2}{S^2}\,, \\ d\omega_2 &= \frac{a_1 \cos\theta_1}{S^2}\,. \end{aligned} \tag{2.4}$$

Here, θ is the angle between the normal of the surface elements and the line of length S joining them (see Fig. 2.1). Substituting $d\omega_1$ and $d\omega_2$ in Eq. 2.2 and Eq. 2.3, it then follows that

$$\begin{aligned} W_{a_1 \to a_2} &= \frac{i_1\ a_1 \cos\theta_1\ \ a_2 \cos\theta_2}{S^2}\,, \\ W_{a_2 \to a_1} &= \frac{i_2\ a_2 \cos\theta_2\ \ a_1 \cos\theta_1}{S^2}. \end{aligned} \tag{2.5}$$

So, to calculate the GCF defined as

$$F_{a_1 \to a_2} = \frac{\text{Energy intercepted by } a_2}{\text{Energy leaving } a_1} = \frac{W_{a_1 \to a_2}}{I_1}, \tag{2.6}$$

we need to determine the denominator I [W/m^2] which corresponds to the total diffuse energy leaving a_1 within the entire hemispherical solid angle over a_1 and is of the form

$$I(\theta,\, \phi) = \int_0^{2\pi} \int_0^{\pi/2} i(\theta, \phi)\, \cos\theta\, \sin\theta\, d\theta\, d\phi. \tag{2.7}$$

Based on our assumption, a diffuse-gray surface absorbs a fixed fraction of incident radiation from any direction and at any wavelength and emits radiation that is a fixed fraction of black body radiation for all directions and all wavelengths. However, they can still depend on the surface temperature. An illuminated ideal diffuse-gray reflecting surface will have equal luminance from all directions which lie in the half-space adjacent to the surface. So, for a diffuse surface, emission is isotropic ($i(\theta, \phi) = i$) and Eq. 2.7 can be rewritten as

$$I = i \int_0^{2\pi} \int_0^{\pi/2} \cos\theta\, \sin\theta\, d\theta\, d\phi = \pi\, I. \tag{2.8}$$

Substituting I from Eq. 2.8 in Eq. 2.6, the geometric configuration factors are of the form

$$F_{a_1 \to a_2} = \frac{W_{a_1 \to a_2}}{\pi\, I_1\, a_1} = \frac{\cos\theta_1\ \cos\theta_2}{\pi\, S^2} a_2\,, \tag{2.9}$$

and vise versa in an analogous manner,

$$F_{a_2 \to a_1} = \frac{W_{a_2 \to a_1}}{\pi\, I_2\, a_2} = \frac{\cos\theta_1\, \cos\theta_2}{\pi\, S^2} a_1, \tag{2.10}$$

where $\pi\, I_1\, a_1$ ($\pi\, I_2\, a_2$) is the total energy leaving a_1 (a_2) within the entire hemispherical solid angle over a_1 (a_2). Using $\mathrm{d}\omega_1$ and $\mathrm{d}\omega_2$ definitions from Eq. set 2.4, the GCF's can be rewritten in the short form

$$\begin{aligned} F_{a_1 \to a_2} &= \frac{\cos\theta_1\, \mathrm{d}\omega_1}{\pi}\,, \\ F_{a_2 \to a_1} &= \frac{\cos\theta_2\, \mathrm{d}\omega_2}{\pi}\,. \end{aligned} \tag{2.11}$$

Then, a reciprocity equation for differential-element configuration factors would be achievable by multiplying Eq. 2.9 by a_1 and Eq. 2.10 by a_2 as

$$a_1\, F_{a_1 \to a_2} = a_2\, F_{a_2 \to a_1}. \tag{2.12}$$

2.3 GCF between a differential element and a finite area

GCF calculation between an isothermal diffuse finite surface area A and an isothermal diffuse infinitesimal surface element a is addressed. There are two GCF's to be determined: first, the GCF from the differential area a to the finite area A, $F_{a \to A}$, and the second one from the finite area A to the differential area a, $F_{A \to a}$. To derive both, we note that the total radiation leaving a is of the form

$$I_a = \pi\, i_a\, a\,, \tag{2.13}$$

and the total radiation leaving A is

$$I_A = \int_A \pi\, i_A\, \mathrm{d}A\,. \tag{2.14}$$

Also, the energy reaching $\mathrm{d}A$ on A from a can be written as

$$W_{a \to \mathrm{d}A} = \int_A i_a\, \frac{\cos\theta_a\, \cos\theta_A}{S^2}\, a\, \mathrm{d}A\,, \tag{2.15}$$

and the energy reaching a from A can be written as

$$W_{A\to a} = a \int_A i_A \frac{\cos\theta_a \, \cos\theta_A}{S^2} \, \mathrm{d}A. \tag{2.16}$$

The GCF $F_{a\to A}$ and $F_{A\to a}$ are then the ratios of $W_{a\to \mathrm{d}A}/I_a$ and $W_{A\to a}/I_A$, respectively:

$$\begin{aligned} F_{a\to A} &= \int_A \frac{\cos\theta_a \, \cos\theta_A}{\pi \, S^2} \, \mathrm{d}A \,, \\ F_{A\to a} &= \frac{a}{A} \int_A \frac{\cos\theta_a \, \cos\theta_A}{\pi \, S^2} \, \mathrm{d}A \,. \end{aligned} \tag{2.17}$$

From Eq. 2.17 the reciprocity for configuration factors between infinitesimal and finite areas can be written as

$$a \, F_{a\to A} = A \, F_{A\to a} \,. \tag{2.18}$$

To accomplish the numerical integration, a dense mesh grid set $\{\mathrm{d}A\}$ is needed to be superposed on finite surface area A. The numerical results need to be mesh independent, using a surface discretization where each subsurface is smaller than the total area of the finite surface by orders of magnitude.

2.4 GCF between two finite areas

Finally, for the case of GCF between two isothermal diffuse finite surface areas A_1 and A_2, the GCF expression would be addressed. Definition $F_{A_1\to A_2}$ denotes the fraction of energy leaving A_1 that arrives at A_2, and vise versa, $F_{A_2\to A_1}$ denotes the fraction of energy leaving A_2 that arrives at A_1. We note that the total radiation leaving A_1 and A_2 are of the forms

$$\begin{aligned} I_1 &= \pi \, i_1 \, A_1 \,, \\ I_2 &= \pi \, i_2 \, A_2 \,. \end{aligned} \tag{2.19}$$

Table 2.1: Summary of geometric configuration factor and reciprocity relation.

Case	Geometric configuration factor	Reciprocity
1	$F_{a_1 \to a_2} = \frac{\cos\theta_1 \, \cos\theta_2}{\pi \, S^2} a_2$	$a_1 \, F_{a_1 \to a_2} = a_2 \, F_{a_2 \to a_1}$
2	$F_{a \to A} = \int_A \frac{\cos\theta_a \, \cos\theta_A}{\pi \, S^2} \, \mathrm{d}A$	$a \, F_{a \to A} = A \, F_{A \to a}$
3	$F_{A_1 \to A_2} = \frac{1}{A_1} \int_{A_1} \int_{A_2} \frac{\cos\theta_1 \, \cos\theta_2}{\pi \, S^2} \, \mathrm{d}A_2 \, \mathrm{d}A_1$	$A_1 \, F_{A_1 \to A_2} = A_2 \, F_{A_2 \to A_1}$

Also, the energy reaching A_2 from A_1 and the energy reaching A_1 from A_2 are respectively given by

$$\begin{aligned} W_{A_1 \to A_2} &= \int_{A_1} \int_{A_2} i_1 \, \frac{\cos\theta_1 \, \cos\theta_2}{S^2} \, \mathrm{d}A_2 \, \mathrm{d}A_1 \, , \\ W_{A_2 \to A_1} &= \int_{A_2} \int_{A_1} i_2 \, \frac{\cos\theta_1 \, \cos\theta_2}{S^2} \, \mathrm{d}A_1 \, \mathrm{d}A_2 \, . \end{aligned} \tag{2.20}$$

The GCF $F_{A_1 \to A_2}$ and $F_{A_2 \to A_1}$ are then the ratio of $W_{A_1 \to A_2}/I_1$ and $W_{A_2 \to A_1}/I_2$, respectively,

$$\begin{aligned} F_{A_1 \to A_2} &= \frac{1}{A_1} \int_{A_1} \int_{A_2} \frac{\cos\theta_1 \, \cos\theta_2}{\pi \, S^2} \, \mathrm{d}A_2 \, \mathrm{d}A_1 \, , \\ F_{A_2 \to A_1} &= \frac{1}{A_2} \int_{A_2} \int_{A_1} \frac{\cos\theta_1 \, \cos\theta_2}{\pi \, S^2} \, \mathrm{d}A_1 \, \mathrm{d}A_2 \, . \end{aligned} \tag{2.21}$$

From equation set 2.21 the reciprocity for configuration factor between two isothermal diffuse finite surface areas can be written as,

$$A_1 \, F_{A_1 \to A_2} = A_2 \, F_{A_2 \to A_1} \, . \tag{2.22}$$

For the sake of simplicity, the relations demonstrated in sections 2.2, 2.3 and 2.4, are listed in Table 2.1.

2.5 Geometric configuration factor features

Known GCF features are listed as follows:

1. Bounding: GCF's are bounded to $0 \leq F \leq 1$ (i.e. the GCF is the fraction of energy exiting from a surface area that impinges on another surface area).

2. Closeness: Consider the GCF's among surfaces that form a complete enclosure. For an enclosure of N surface areas the entire energy leaving from any single surface A_i must be incident on all the surfaces forming the enclosure. So, summing up all geometric configuration factors from a given surface in an enclosure must equal 1;

$$\sum_{j=1}^{N} F_{i\to j} = 1 \, . \tag{2.23}$$

3. Algebra: Consider A_1 and A_2 two isothermal surface areas exchanging energy based on geometric configuration factors $F_{1\to 2}$ and $F_{2\to 1}$. If A_2 is divided into two parts A_3 and A_4 the GCF from A_1 to A_2 would be of the form

$$F_{A_1\to A_2} = F_{A_1\to A_3} + F_{A_1\to A_4} \, . \tag{2.24}$$

2.6 GCF numerical integration

As it was shown in previous sections, the evaluation of the configuration factors requires integration over the finite areas involved. In the absence of exact analytical expression for geometric configuration factors of arbitrary geometries, tedious numerical integration is required. To accomplish a precise numerical integration, a set of dense mesh grids is needed to be superposed on finite surface areas. The numerical results need to be mesh independent, using a surface discretization where each subsurface is smaller than the total area of the finite surface by orders of magnitude. Geometric configuration factor features are useful tools for increasing the speed or accuracy of these computations. These techniques will be discussed and applied in following chapters. Also, a number of methods are available for increasing the speed and accuracy of the GCF calculation in [72, 73]. However, many configuration factors for specific geometries have been given in analytical form and have been spread throughout the literature. A detailed selection of the GCF formulation also has been given by [74].

2.7 Diffuse-gray enclosure

An assumption in this study to ensure that all radiative contributions are accounted for is that simulated material is enclosed by a fiducial volume (see Fig. 2.2) whose boundary walls are composed of different or the same material. The surfaces are assumed to be diffuse and gray such that the emissivity and absorptivity do not depend on direction or wavelength. The emissivity and absorptivity are equal and only depend on surface temperature. Even though this assumption is valid to be considered by only a limited number of real materials, the diffuse-gray approximation simplifies the simulation greatly.

Surfaces of enclosure can have various imposed thermal boundary conditions. In the simplest case, all surfaces are isothermal. However, if the boundary conditions imposed on the analysis are such that the temperature needs to vary remarkably over an area, the area can be readily subdivided into smaller isothermal portions. Also, the surfaces of the enclosure are either taken to be perfectly insulated from external heat addition and removal or in exchange of energy with external thermal sources. Two widely used conditions which are imposed in this thesis are illustrated schematically in Fig. 2.3. Symmetric condition denotes that the energy fluxes incoming to and outgoing from a surface area are equal. The asymmetric condition denotes that the difference between incoming and outgoing energy fluxes are not zero and a fraction of radiation is absorbed by the surface area.

The accuracy of the results is a further consideration which needs to be addressed. The accuracy of the results is strongly dependent on the number of enclosure surface areas. A poor accuracy is possible if too few areas are designated such that significant non-uniformity in reflected flux over an area has not been accounted for. On the other hand, too many areas require excessive computation time. An engineering judgment is required to define a "figure of merit" for the selection of an optimal number of

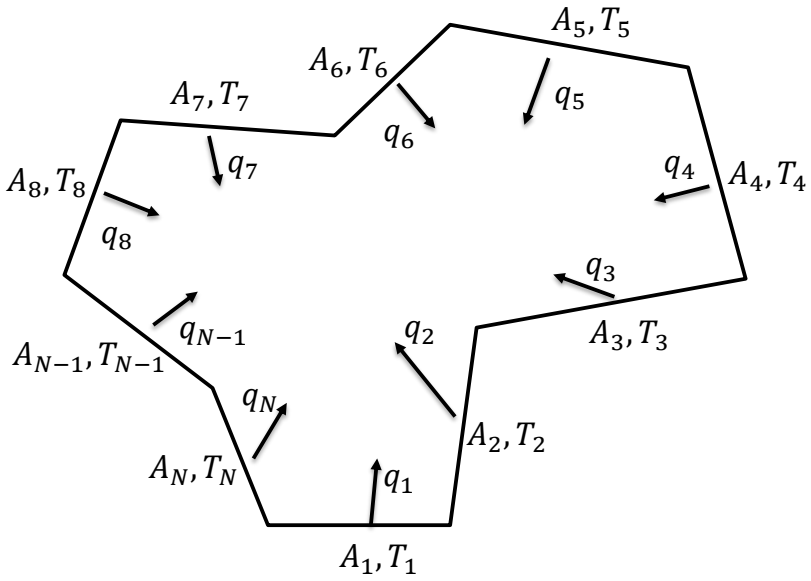

Figure 2.2: Enclosure composed of N diffuse-gray isothermal surfaces of area A and at temperature T. The surface areas emit energy flux q and are assumed to be insulated from external energy exchanges.

subsurface area elements.

2.8 Radiation exchange model

For the purpose of this study, consider an enclosure composed of some discrete surface areas. Each surface is identified by area A_i and assigned to be at temperature T_i. Subscript i refers to the i^{th} face. All surfaces within the fiducial volume produce a complex system of radiation exchange. Each unit surface area A radiates across all wavelengths per unit time due to the temperature of that particular surface element. The emitted energy from each surface area is propagated by rays which are released in all directions (diffuse-gray model) through straight lines. These rays travel through the fiducial volume and transfer energy to the other surface areas. The radiation sent from a surface element is partially intercepted and reflected when another surface is encountered. This process is repeated multiple times through all surfaces.

To formulate the energy exchange process, the diffuse-gray net radiation method

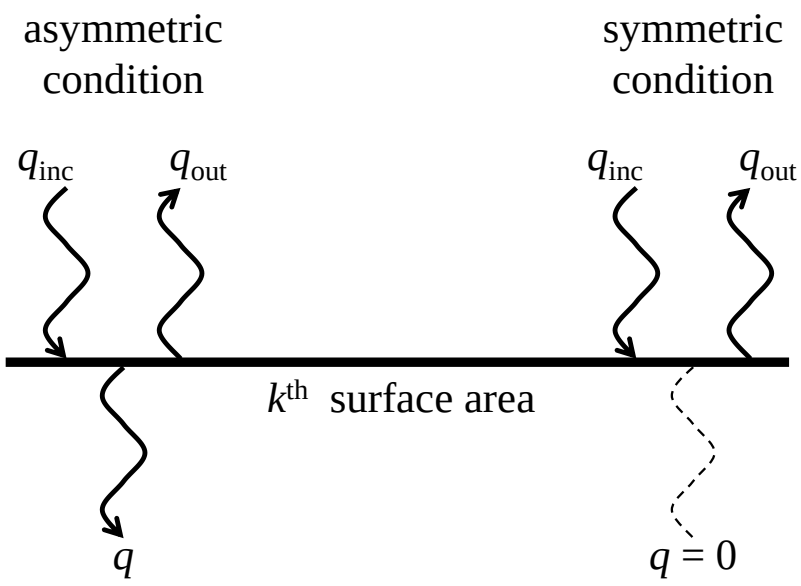

Figure 2.3: Schematic explanation of the asymmetric and symmetric condition at the k-th surface area.

[61] is used. The goal is to analyze the radiation exchange between the surface areas (in total N surfaces) in discretized time step. To formulate this complex energy exchange process we use the *net-radiation method*.

Consider the i^{th} surface to be at temperature T_i and the quantities $q_{\text{out},\,i}$ [W m^{-2}] and $q_{\text{inc},\,i}$ [W m^{-2}] be the rates of outgoing and incoming radiant energy per unit area, respectively. We will recall $q_{\text{out},\,i}$ and $q_{\text{inc},\,i}$, hereafter, *radiosity* and *incident radiation*. From the Stefan-Boltzmann law the rate of energy emitted per unit area of the i^{th} surface (gray body) is proportional to the fourth power of its temperature,

$$q_{\text{out},\,i} = \epsilon\,\sigma\,T_i^4, \tag{2.25}$$

where ϵ is the emissivity of the gray body (if it is a perfect black-body $\epsilon = 1$) and σ denotes the Stefan-Boltzmann constant [W m^{-2} K^{-4}]. From the fact that the energy flux leaving the surface is composed of emitted plus reflected energy, a second term must be added to equation 2.25. So, the radiosity $q_{\text{out},\,i}$, for a gray-diffuse surface, is the sum of the reflected and emitted irradiances as follows,

$$q_{\text{out},\,i} = \epsilon\,\sigma\,T_i^4 + (1-\epsilon)\,q_{\text{inc},\,i}\,. \tag{2.26}$$

It then follows that, the incident energy flux of the i^{th} surface, $q_{\text{inc},\,i}$, is determined by summing over the portions of the radiation leaving other enclosure surfaces which arrive at the i^{th} surface:

$$\frac{F_{j\,i}\,A_j}{A_i}\,q_{\text{out},\,j}\,. \tag{2.27}$$

So, the incident irradiance $q_{\text{inc},\,i}$ is the sum of radiation from all other surfaces per unit area A_i and is of the form,

$$q_{\text{inc},\,i} = \frac{\sum_{j=1}^{N}\left(F_{j\,i}A_j q_{\text{out},\,j}\right)}{A_i}, \tag{2.28}$$

where $F_{j\,i}$ is the predefined geometric configuration factor from surface j to surface i. Now, employing the reciprocity relation equation

$$A_j F_{j\,i} = A_i F_{i\,j}, \tag{2.29}$$

Eq. 2.28 is rewritten in the form

$$q_{\text{inc},\,i} = \sum_{j=1}^{N} F_{i\,j}\,q_{\text{out},\,j}\,. \tag{2.30}$$

Then, substituting the incident irradiance Eq. 2.30 into the Eq. 2.26, for the i^{th} surface area we get

$$q_{\text{out},\,i} = \epsilon\,\sigma\,T_i^4 + (1-\epsilon)\sum_{j=1}^{N} F_{i\,j}\,q_{\text{out},\,j}. \tag{2.31}$$

The equation 2.31 is the balance between net radiative loss and energy supplied by the radiation inside the enclosure. We assumed there is no neither external energy source nor leakage of energy (i.e. the enclosure surfaces are isolated).

For an N surface area, this summation for each surface will generate N linear equations with N unknown radiosities. It then follows that we can construct a $N \times N$ system of linear equations for the set $\{q_{\text{out},\,i}\}_{i=1}^{N}$ as follows

$$q_{\text{out},\,i} - (1-\epsilon)\sum_{j=1}^{N} F_{i\,j}\,q_{\text{out},\,j} = \epsilon\,\sigma\,T_i^4, \qquad i = 1,\ldots,N\,. \tag{2.32}$$

The temperature T_i are known (i.e., initialized) quantities, and the F_{ij} are calculated previously. The resulting $N \times N$ system of linear equations can then be readily solved via standard numerical methods (e.g., Gaussian elimination). It then follows that the incident radiation $\{q_{\text{inc},\,i}\}_{i=1}^{N}$ can be explicitly calculated from Eq. 2.30. Once the radiosities and incident radiations have been calculated, the net heat transfer q_i at i^{th} surface can be determined by finding the difference between the incoming and outgoing energy (asymmetric condition Fig. 2.3) as follows,

$$q_i = q_{\text{inc},\,i} - q_{\text{out},\,i}. \tag{2.33}$$

2.9 Radiation heat conductivity model

Most of the materials have physical and mechanical properties which differ with orientation [81]. The geometric configuration factor is the quantity of importance to investigate the anisotropic behavior of the model. A non-uniform distribution of the GCF's, with considering the explicit dependence of energy exchange process on geometry configuration factors, introduces an anisotropic property. One of these properties is radiative conductivity κ. Therefore, radiative conductivity is expected to vary with orientation. For anisotropic cases, κ is represented by a 3×3 matrix with elements $\kappa_{m\,n}$, where m and n denote the Cartesian coordinates x, y, and z. The most well known approach to address the anisotropic behavior of the radiation heat conductivity is based on the use of the law of heat conduction (Fourier's law). The law of heat conduction states that the time rate of heat transfer through a material is proportional to the negative gradient in the temperature and to the area, at right angles to that gradient, through which the heat flows. So, considering q_n as the heat flux in a direction n, which is normal to an isotherm, therefore, in Cartesian coordinates, the heat flux vector $\vec{q}$ can be resolved into components such that in a

directional expression it can be expressed as follows,

$$\vec{q} = q_x \, \hat{i} + q_y \, \hat{j} + q_z \, \hat{k}. \tag{2.34}$$

It then follows the differential form of Fourier's law shows that the local heat flux density is equal to the product of thermal conductivity and the negative local temperature gradient as follows,

$$\vec{q} = -\kappa \, \vec{\nabla} T \tag{2.35}$$

and in a matrix form,

$$\begin{pmatrix} q_x \\ q_y \\ q_z \end{pmatrix} = - \begin{pmatrix} \kappa_{x\,x} & \kappa_{x\,y} & \kappa_{x\,z} \\ \kappa_{y\,x} & \kappa_{y\,y} & \kappa_{y\,z} \\ \kappa_{z\,x} & \kappa_{z\,y} & \kappa_{z\,z} \end{pmatrix} \begin{pmatrix} \frac{\partial T}{\partial x} \\ \frac{\partial T}{\partial y} \\ \frac{\partial T}{\partial z} \end{pmatrix}. \tag{2.36}$$

$\partial/\partial x$, $\partial/\partial y$ and $\partial/\partial z$ denote gradient operator along x, y and z component, respectively, and the diagonal elements $\kappa_{i\,i}$ are radiative conductivity along the main axes.

Chapter 3

FiberForm® simulation using artificial geometries

3.1 Introduction

In this chapter, a simplified three-dimensional direct simulation model is developed. The model is used to study the effective radiative conductivity of fibrous material using a geometry with properties resembling those of carbon-preform. Since the fibrous material is a low-density (high porosity) composite made from rigid carbon fibers, simulations are carried out using artificial non-overlapped perfect cylinders with arbitrary size and orientation. Then, using a Monte-Carlo procedure the perfect cylinders are irregularly positioned within a 3D cubic enclosure (fiducial volume) until the desired fiber volume fraction is obtained. This ultimately will resulte in a heterogeneous distribution of the cylinders, resembling anisotropic properties of the FiberForm®. After the fiducial volume simulation is completed, gray body diffuse radiation and radiation heat conductivity models are applied to analyze the heat transfer process. It is shown that the effective radiative conductivity is a function of both temperature and the orientation of the fibers. The model results are validated

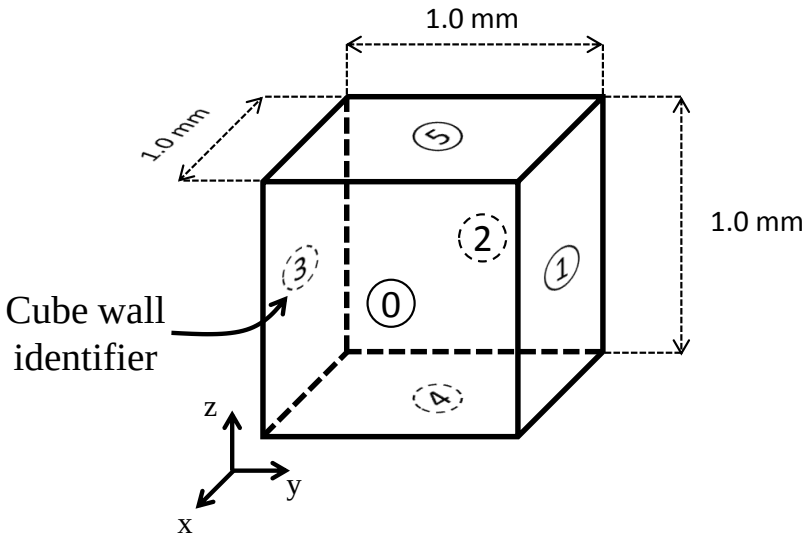

Figure 3.1: Schematic Figure of the specific experimental geometry employed in the model. The fiducial volume consists of a cubic enclosure whose boundary walls are composed of the same material as the inside fibers. The integers are used to identify the boundary surfaces.

by comparing them with numerical studies of a transient volume averaged heat model.

3.2 Model

While X-ray micro-tomography measurements of FiberForm® [64] show that the overall geometry of the actual fibers is not perfectly cylindrical, the high porosity of the material makes the cylindrical geometry appropriate for validation studies. As illustrated schematically in Fig. 3.1, the measurement volume, or fiducial volume, used in the present analysis is assumed to be a cubic enclosure, 1.0 mm (x) × 1.0 mm (y) × 1.0 mm (z), which contains the arbitrarily sized, positioned, and oriented cylinders. Therefore, the fibers are treated as perfect cylinders and are generated in two steps as follows.

First, a set of arbitrary values for the radius and length, $\{r_i\}_{i=1}^{M}$ and $\{h_i\}_{i=1}^{M}$, are assigned to M cylinders. In Cartesian coordinates, if the cylinders are generally oriented along the z-axis $(0, 0, 1)$, then the centers of the bottom and top cap of the

i^{th} fiber are

$$\mathbf{P}_{b,\,i} = \begin{pmatrix} 0 \\ 0 \\ -h_i/2 \end{pmatrix}, \qquad \mathbf{P}_{t,\,i} = \begin{pmatrix} 0 \\ 0 \\ h_i/2 \end{pmatrix}, \tag{3.1}$$

respectively.

Secondly, the fibers within the 3D geometry (fiducial volume) are rotated and translated using a linear transformation mapping, $\mathfrak{T}\mathfrak{r}(\mathbf{x}) = \mathbf{x}'$. Rotation and translation are accomplished by using a pair of operators, called the rotation and translation operators.

First, three arbitrary angles ($0 \leq \alpha,\, \beta,\, \gamma \leq 2\pi$) are chosen each defines a rotation operator associated to each angle to rotate the main axis of the cylinders. The singular rotations in matrix form are expressed as

$$\mathcal{R}_{\gamma(z)} = \begin{pmatrix} \cos\gamma & -\sin\gamma & 0 \\ \sin\gamma & \cos\gamma & 0 \\ 0 & 0 & 1 \end{pmatrix}, \tag{3.2}$$

$$\mathcal{R}_{\beta(y)} = \begin{pmatrix} \cos\beta & 0 & \sin\beta \\ 0 & 1 & 0 \\ -\sin\beta & 0 & \cos\beta \end{pmatrix}, \tag{3.3}$$

$$\mathcal{R}_{\alpha(x)} = \begin{pmatrix} 1 & 0 & 0 \\ 0 & \cos\alpha & -\sin\alpha \\ 0 & \sin\alpha & \cos\alpha \end{pmatrix}. \tag{3.4}$$

Then, the rotation operator $\mathcal{R}$ would be an extrinsic rotation defined as three matrix multiplications and expressed as

$$\mathcal{R} = \mathcal{R}_{\gamma(z)}\, \mathcal{R}_{\beta(y)}\, \mathcal{R}_{\alpha(x)}, \tag{3.5}$$

where α, β, γ are predefined random Euler angles about the x-, y-, z-axes, respectively. So, we get

$$\mathcal{R} = \begin{pmatrix} \mathcal{R}_{11} & \mathcal{R}_{12} & \mathcal{R}_{13} \\ \mathcal{R}_{21} & \mathcal{R}_{22} & \mathcal{R}_{23} \\ \mathcal{R}_{31} & \mathcal{R}_{32} & \mathcal{R}_{33} \end{pmatrix} . \tag{3.6}$$

R_{mn} are rotation matrix elements and are of the form,

$$\begin{aligned} \mathcal{R}_{11} &= \cos\beta\cos\gamma\,, \\ \mathcal{R}_{12} &= \cos\gamma\sin\alpha\sin\beta - \cos\alpha\sin\gamma\,, \\ \mathcal{R}_{13} &= \cos\alpha\cos\gamma\sin\beta + \sin\alpha\sin\gamma\,, \\ \mathcal{R}_{21} &= \cos\beta\sin\gamma\,, \\ \mathcal{R}_{22} &= \cos\alpha\cos\gamma + \sin\alpha\sin\beta\sin\gamma\,, \\ \mathcal{R}_{23} &= -\cos\gamma\sin\alpha + \cos\alpha\sin\beta\sin\gamma\,, \\ \mathcal{R}_{31} &= -\sin\beta\,, \\ \mathcal{R}_{32} &= \cos\beta\sin\alpha\,, \\ \mathcal{R}_{33} &= \cos\alpha\cos\beta\,. \end{aligned} \tag{3.7}$$

A rotation operator is assigned for each cylinder as $\mathcal{R}_i$. Therefore, the main axis rotate to:

$$\mathbf{v} = \mathcal{R}\begin{pmatrix} 0 \\ 0 \\ 1 \end{pmatrix} = \begin{pmatrix} \mathcal{R}_{13} \\ \mathcal{R}_{23} \\ \mathcal{R}_{33} \end{pmatrix} \tag{3.8}$$

Moreover, we need to move all the cylinders to their arbitrary locations in space by using a translation operator $\mathcal{T}$ which will be defined arbitrary for each cylinder in the form of,

$$\mathcal{T}\begin{pmatrix} x \\ y \\ z \end{pmatrix} = \begin{pmatrix} x + x_0 \\ y + y_0 \\ z + z_0 \end{pmatrix} . \tag{3.9}$$

Finally, rotation operator $\mathcal{R}$ and translation operator $\mathcal{T}$ are combined to form the transform operator $\mathfrak{T}\mathfrak{r} = \mathcal{T}\,\mathcal{R}$. The transform operator modifies the observation point $\mathbf{x} = (x, y, z)$ as follows,

$$\mathbf{x}' = \mathfrak{T}\mathfrak{r}(\mathbf{x}) = \begin{pmatrix} x_0 \\ y_0 \\ z_0 \end{pmatrix} + \begin{pmatrix} \mathcal{R}_{11} & \mathcal{R}_{12} & \mathcal{R}_{13} \\ \mathcal{R}_{21} & \mathcal{R}_{22} & \mathcal{R}_{23} \\ \mathcal{R}_{31} & \mathcal{R}_{32} & \mathcal{R}_{33} \end{pmatrix} \begin{pmatrix} x \\ y \\ z \end{pmatrix}, \tag{3.10}$$

Again, a transform operator is assigned for each cylinder which transforms top and bottom cap of the i^{th} cylinder as follows respectively

$$\mathbf{P}_b = \mathfrak{T}\mathfrak{r} \begin{pmatrix} 0 \\ 0 \\ \frac{-h}{2} \end{pmatrix} = \begin{pmatrix} x_0 - \frac{h}{2}\mathcal{R}_{13} \\ y_0 - \frac{h}{2}\mathcal{R}_{23} \\ z_0 - \frac{h}{2}\mathcal{R}_{33} \end{pmatrix}, \tag{3.11}$$

$$\mathbf{P}_t = \mathfrak{T}\mathfrak{r} \begin{pmatrix} 0 \\ 0 \\ \frac{h}{2} \end{pmatrix} = \begin{pmatrix} x_0 + \frac{h}{2}\mathcal{R}_{13} \\ y_0 + \frac{h}{2}\mathcal{R}_{23} \\ z_0 + \frac{h}{2}\mathcal{R}_{33} \end{pmatrix}. \tag{3.12}$$

So, each cylinder is defined by bottom $\mathbf{P}_b$ and top $\mathbf{P}_t$ caps center position, radius r and unit vector $\mathbf{v}$ as the cylinder main axis (see Fig. 3.2). The geometrical properties of the fiber used here have a radius of $10.0 \leq r \leq 20.0$ [μm] and a length of $300.0 \leq h \leq 600.0$ [μm]. The cylinders with random sizes and orientations are positioned irregularly within the fiducial volume until the desired fiber volume fraction of $\simeq 0.2$ is obtained.

A preferred orientation applied to the cylinders makes the simulation more realistic. The cylinders are simulated such that each cylinder has an azimuthal direction oriented between $-15.0^\circ < \xi < 15.0^\circ$ with respect to the xy-plane. This condition is achieved if and only if the angle between the each cylinder main axis $\mathbf{v}$ and normal to the xy-plane $\hat{k}$ satisfies,

$$\sin^{-1}\left(\left|\hat{k} \cdot \mathbf{v}\right|\right) \leq 15.0^\circ. \tag{3.13}$$

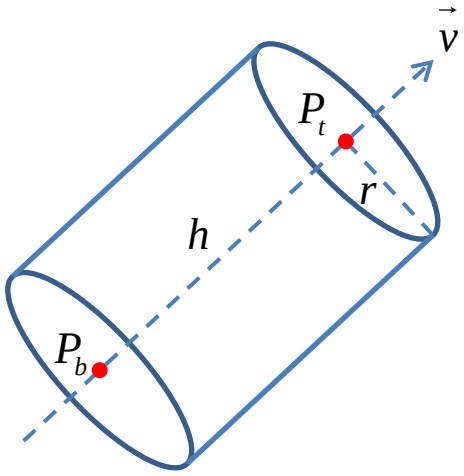

Figure 3.2: Schematic illustration of a cylinder defined via radius r, length h, main axis $\mathbf{v}$ and the bottom and top caps center coordinates $\mathbf{P}_b$ and $\mathbf{P}_t$, respectively.

This preferred orientation is expected to reduce the thermal conductivity in z-direction.

3.3 Non-overlapping cylinders test

The FiberForm® will be modeled as a random array of non-overlapping cylinders to prevent any heat transfer by conduction. The non-overlapping condition is verified using the separating axes method [78]. As an aid to the interested reader we briefly explain this method.

Separating axis method in 2D has been illustrated in Fig. 3.3 between two "a" and "b" objects. This is a method to determine if two convex shapes are intersecting. In particular, the goal is finding a line where the projections of the shapes do not overlap. The corresponding line is called a separation axis. Based on Fig. 3.3, two convex objects do not intersect if there exist a direction $\vec{D}$ such that either

$$\lambda^{(a)}_{min}(\vec{D}) > \lambda^{(b)}_{max}(\vec{D}),$$
$$\text{or} \tag{3.14}$$
$$\lambda^{(a)}_{max}(\vec{D}) < \lambda^{(b)}_{min}(\vec{D}).$$

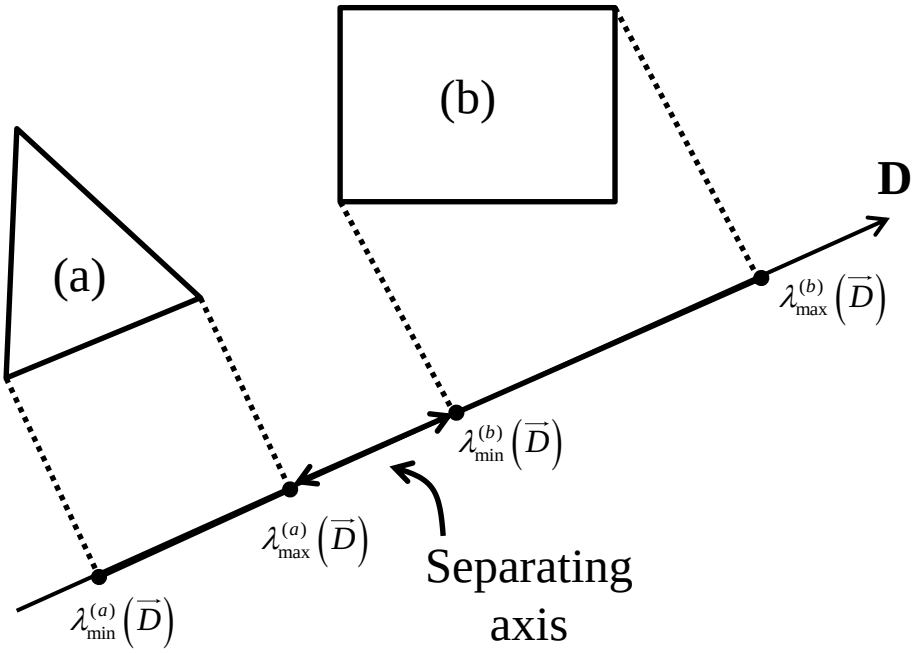

Figure 3.3: Schematic illustration of the separating axes method.

So, via determining λ_{min} and λ_{max} of the projection of two cylinders (carbon fibers) onto a direction $\vec{D}$ and checking the condition 3.14, we are able to define whether two objects are overlapping or not. The direction $\vec{D}$ can be chosen from one of following,

1. Separation tests involving the cylinder axis directions.

2. Separation tests involving the cylinder axis perpendiculars.

3. Separation tests involving other directions.

The algorithm regarding to the separating axis method is roughly expensive numerically. An alternative method can be proposed such that minimum distance between the cylinder main axes be smaller or equal to the sum of the cylinder radii. It should be noted that, by using this test we are using imaginary capsule shape instead of cylindrical shape. However, we preferred to use the expensive test to obtain a more realistic simulation of the material.

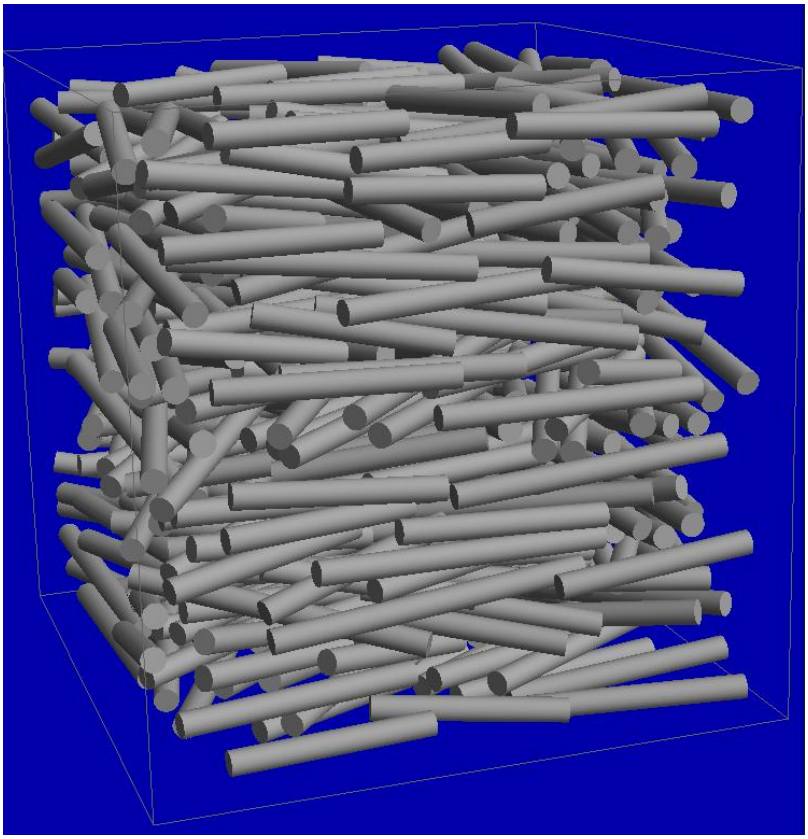

Figure 3.4: (Color online) Artificial FiberForm®. The boundary surfaces illustrated in Fig. 3.1 are not illustrated here.

Finally, the geometrical layout of the cylindrical fibers used in the present analysis are presented in Fig. 3.4, where non-overlapped simulated perfect cylinders, irregularly oriented to be at angle $< |15.0°|$ with respect to the xy-plane, within the cubic fiducial volume. Porosity $\phi \simeq 0.8$ has been obtained via arbitrary sized fibers.

3.4 Mesh grid generqator

Efforts to develop an analytical approximation for calculating the geometric configuration factor of two cylinders of the same geometry and different orientations has been done in Ref. [79]. Here, we explicitly determine the GCF of the perfect cylinders which have different geometries and orientations using the numerical calculation of Eq. 2.21. Numerical determination of the GCF requires a planar discretization of

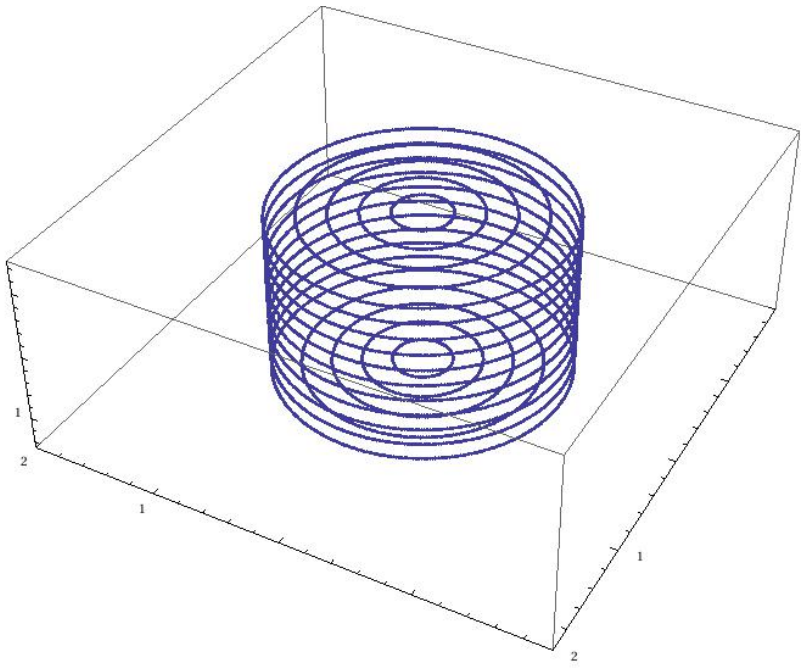

Figure 3.5: schematic illustration of the mesh surface area on the surface of a cylindrical fiber. The blue dots denote the centroid of the surface area elements.

fiber perimeter containing a set of grids illustrated schematically in Fig. 3.5.

In first step we generate the mesh grid on surface of an imaginary cylinder at the origin of our appropriate Coordinate system as follows,

$$\begin{aligned} x &= r\cos\phi\ , \\ y &= r\sin\phi\ , \\ z &= z\ , \end{aligned} \tag{3.15}$$

where $z \in [-h/2 + \delta z,\, h/2 - \delta z]$ incremented by δz and $\phi \in [0,\, 2\pi]$ incremented by $\delta\phi$. Also, for the top and bottom caps mesh grid, we use

$$\begin{aligned} x &= \rho\cos\phi\ , \\ y &= \rho\sin\phi\ , \\ z &= -\frac{h}{2} \quad \text{or} \quad \frac{h}{2}, \end{aligned} \tag{3.16}$$

where $\rho \in [0,\, r]$ incremented by $\delta\rho$ and $\phi \in [0,\, 2\pi]$ incremented by $\delta\phi\, r/\rho$.

Acting predefined transform operator $\mathfrak{Tr}$ on the generated mesh grid, each mesh grid points, it is easy then to transform them to the locations specified for each

cylinder as follows,

$$\begin{pmatrix} x_{tr} \\ y_{tr} \\ z_{tr} \end{pmatrix} = \mathfrak{Tr} \begin{pmatrix} x \\ y \\ z \end{pmatrix} = \begin{pmatrix} x_0 \\ y_0 \\ z_0 \end{pmatrix} + \begin{pmatrix} \mathcal{R}_{11} & \mathcal{R}_{12} & \mathcal{R}_{13} \\ \mathcal{R}_{21} & \mathcal{R}_{22} & \mathcal{R}_{23} \\ \mathcal{R}_{31} & \mathcal{R}_{32} & \mathcal{R}_{33} \end{pmatrix} \begin{pmatrix} x \\ y \\ z \end{pmatrix}, \tag{3.17}$$

then we get

$$\begin{pmatrix} x_{tr} \\ y_{tr} \\ z_{tr} \end{pmatrix} = \begin{pmatrix} x_0 + x\mathcal{R}_{11} + y\mathcal{R}_{12} + z\mathcal{R}_{13} \\ y_0 + x\mathcal{R}_{21} + y\mathcal{R}_{22} + z\mathcal{R}_{23} \\ z_0 + x\mathcal{R}_{31} + y\mathcal{R}_{32} + z\mathcal{R}_{33} \end{pmatrix}. \tag{3.18}$$

We do note that, the small mesh surface areas on the surface of the cylinder are ultimately the area surrounded by four adjacent mesh grids.

We do note that one limitation of determining the GCF's is that, in general, the accuracy of the results strongly depend upon mesh grid discretization. Therefore, one may wish to use densely-spaced grid points on the surface of the fibers for accurate solutions. Implementing such a densely-spaced mesh grid, in often unacceptably long execution times, would not be possible or practical. On the other hand, implementing coarsely-spaced grid points causes losing accuracy. Thus, we are forced to propose a way to improve the accuracy of the results. Since, our numerical experiment takes place in a closed volume (e.g. cube), we expect the sum over the i^{th} surface configuration factor through the rest of the surfaces follow the closure

$$\sum_{j=1}^{N} F_{ij} \left(1 - \delta_{ij}\right) = 1, \tag{3.19}$$

where, δ_{ij} is Kronecker delta defined as

$$\delta_{ij} = \begin{cases} 1 & \text{if} \quad i = j \\ 0 & \text{if} \quad i \neq j, \end{cases} \tag{3.20}$$

and used since the i^{th} surface assumed to be concave (can not view itself), $F_{ii} = 0$. But, losing accuracy causes a slightly different value in summation, $1 - \epsilon$. In order to compensate the difference, the value ϵ would be distributed, based on the weight of each F_{ij}, among the GCF's such that the summation tends to 1.

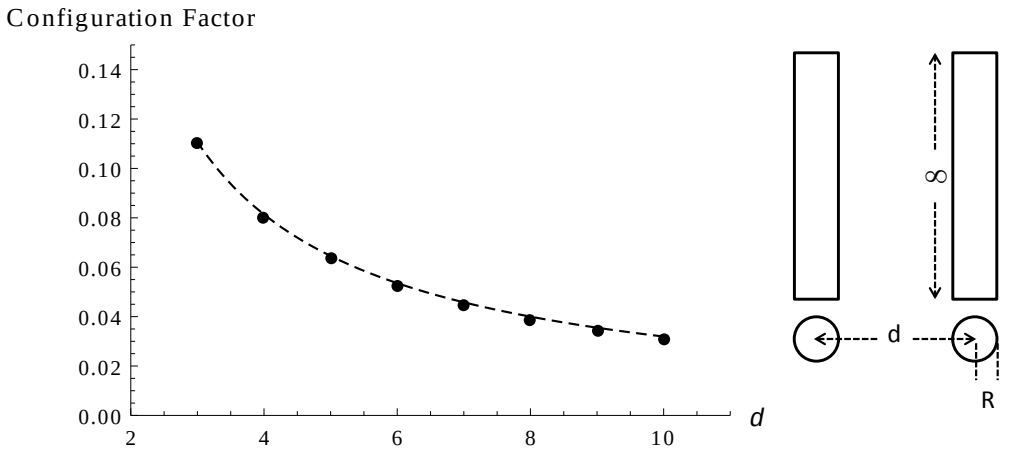

Figure 3.6: Comparison of configuration factors for two infinite-parallel cylinders as a function of interval d between numerical (Data points) and analytical results (solid line) in panel (a). The cylinders configuration is shown in panel (b).

3.5 GCF numerical integration analysis

To evaluate the accuracy of the numerical calculation we compare the numerical results from some particular cases by the analytical results. These comparisons have been plotted in figures 3.6, 3.7 and 3.8. The configuration factor regarding two infinite-parallel cylinders (with same radius and length) are shown in Fig. 3.6 as a function of two cylinders interval, d. The points computed by numerical integration and the solid line is the curve defined by the analytical solution. The numerical and analytical results regarding two finite-parallel cylinders (with same radius and length) have been compared in Fig. 3.7 as a function of two cylinders interval, d. For pure θ-rotations ($\phi = 0$) about the mid-point of one of the cylinders, the GCF's are symmetric with respect to $\theta = 90\,^{\circ}$. Computations were therefore performed for $0 \leq \theta \leq 90\,^{\circ}$. The variation of the GCF's as a function of θ are shown in Fig. 3.8. The points computed by numerical integration and the solid line is the curves defined by the analytical solution.

The comparison between the two methods shows that good agreement is achieved (average relative error $< 3.0\%$). The numerical results are mesh independent, using

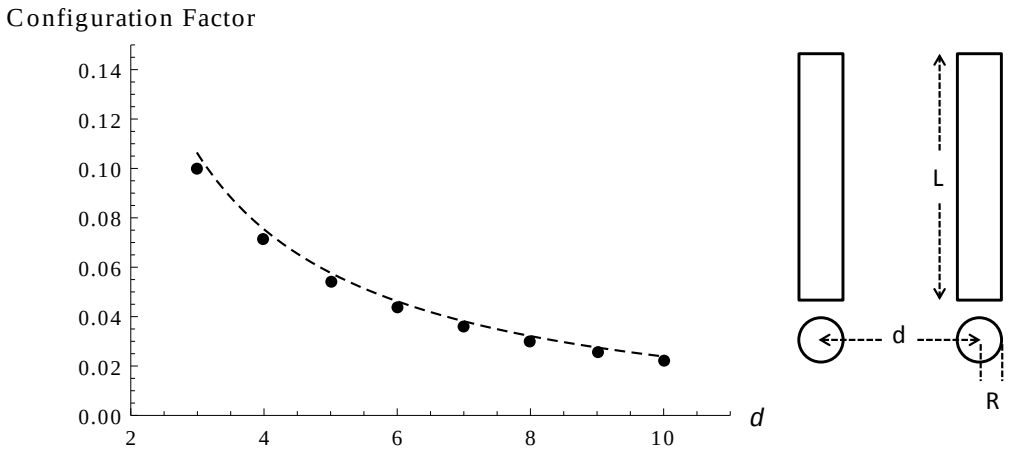

Figure 3.7: Comparison of configuration factors for two finite-parallel cylinders as a function of interval d between numerical (Data points) and analytical results (solid line) in panel (a). The cylinders configuration is shown in panel (b).

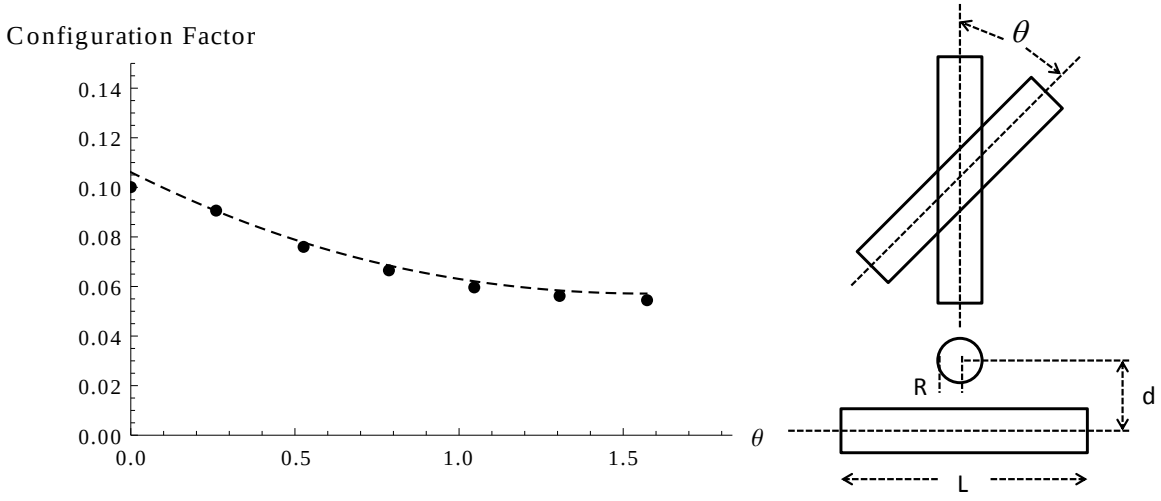

Figure 3.8: Comparison of configuration factors for mid-point θ-rotations between numerical (Data points) and analytical results (solid line) in panel (a). The cylinders configuration is shown in panel (b).

a surface discretization where each sub-surface is smaller than the total area of the cylinder by 6 orders of magnitude, $dA = 10^{-6}A$. With this level of refinement, the numerical approach is expected to produce more accurate results than the analytical approximation. Several other verification test-cases were performed using Ref. [80] but are not presented here.

A histogram of the GCF's, $F_{i,j}$, from the fibers to the internal boundary surfaces of the fiducial volume is shown in Fig. 3.9. A non-uniform distribution of the GCF's,

which considers the explicit dependence of energy exchange process on geometry configuration factors, shows that the model simulates anisotropic properties. Therefore, radiative conductivity, κ, is expected to vary with orientation and use of the law of heat conduction (Fourier's law) discussed in 2.9 is demanded.

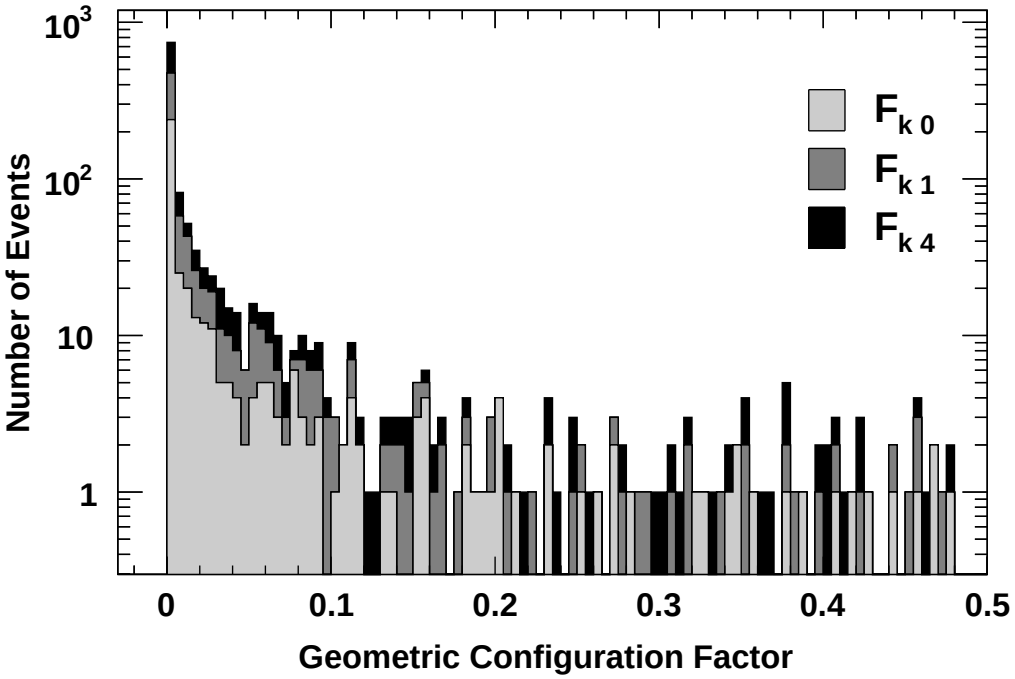

Figure 3.9: Histograms of the calculated geometric configuration factor F_{kj} from the fibers within the fiducial volume (i.e. $k \in \{6, 7, 8, \ldots, N-1\}$) to the selected internal boundary surface (e.g. $j \in \{0, 1, 4\}$) F_{k0} (light-gray), F_{k1} (gray) and F_{k4} (black), respectively.

3.6 Ray-fiber intersection analysis

The emitted energy from the surface element is propagated by rays which are released in all directions (diffuse-gray model) through straight lines. These rays travel through the porous material and transfer energy to the other surface elements if and only if the line does not intersect with another surface element. Hence, the problem of determining whether a line and a surface element in three-dimensions are intersecting needs to be addressed. In the present model, since all fibers are cylindrical, this

process can be greatly accelerated by evaluating the intersection between a line and the whole cylinder, instead of each individual surface element.

3.6.1 Cylinder surface equation

The process starts from the mathematical formulation of the set of surface shape equations for a finite cylinder (without caps) of radius r oriented along $\mathbf{v}$ (from $\mathbf{P}_b$ to $\mathbf{P}_t$), which is of the form:

$$\left\|\mathbf{q}-\mathbf{P}_b-\left(\mathbf{v}\cdot\left(\mathbf{q}-\mathbf{P}_b\right)\right)\mathbf{v}\right\|^2-r^2=0\,, \tag{3.21}$$

$$\mathbf{v}\cdot\left(\mathbf{q}-\mathbf{P}_b\right)>0\,, \tag{3.22}$$

$$\mathbf{v}\cdot\left(\mathbf{q}-\mathbf{P}_t\right)<0\,. \tag{3.23}$$

Here, $\mathbf{q}$ is a point (x,y,z) on the cylinder. Using cylinder main axis, bottom and top caps coordinate predefined in equations 3.8, 3.11 and 3.12, respectively, we can also expand Eq. 3.21 in the form of,

$$\begin{aligned}&\Big(\left(a^2-1\right)(x-x_b)+a\,b\,(y-y_b)+a\,c\,(z-z_b)\Big)^2+\\&\Big(b\,a\,(x-x_b)+\left(b^2-1\right)(y-y_b)+b\,c\,(z-z_b)\Big)^2+\\&\Big(c\,a\,(x-x_b)+c\,b\,(y-y_b)+\left(c^2-1\right)(z-z_b)\Big)^2-r^2=0\,,\end{aligned} \tag{3.24}$$

$$a\,(x-x_b)+b\,(y-y_b)+c\,(z-z_b)>0\,, \tag{3.25}$$

$$a\,(x-x_t)+b\,(y-y_t)+c\,(z-z_t)<0\,. \tag{3.26}$$

Above we assumed,

$$\mathbf{v}=\begin{pmatrix}a\\b\\c\end{pmatrix}\,,\qquad \mathbf{P}_b=\begin{pmatrix}x_b\\y_b\\z_b\end{pmatrix}\,,\qquad \mathbf{P}_t=\begin{pmatrix}x_t\\y_t\\z_t\end{pmatrix}\,. \tag{3.27}$$

The equations governing the bottom and top caps can be expressed respectively

as follows,

$$\mathbf{v} \cdot \left(\mathbf{q} - \mathbf{P}_b\right) = 0\,, \tag{3.28}$$

$$\|\mathbf{q} - \mathbf{P}_b\|^2 < r^2\,, \tag{3.29}$$

$$\mathbf{v} \cdot \left(\mathbf{q} - \mathbf{P}_t\right) = 0\,, \tag{3.30}$$

$$\|\mathbf{q} - \mathbf{P}_t\|^2 < r^2\,. \tag{3.31}$$

Then, the expanded form, respectively, would be of the form,

$$a\,(x - x_b) + b\,(y - y_b) + c\,(z - z_b) = 0\,, \tag{3.32}$$

$$(x - x_b)^2 + (y - y_b)^2 + (z - z_b)^2 < r^2\,, \tag{3.33}$$

$$a\,(x - x_t) + b\,(y - y_t) + c\,(z - z_t) = 0\,, \tag{3.34}$$

$$(x - x_t)^2 + (y - y_t)^2 + (z - z_t)^2 < r^2\,. \tag{3.35}$$

3.6.2 Finite Cylinder – Ray Intersection

From basic radiation physics, since the radiation beams will travel between source and target through a straight line, it is clear then in GCF calculation only the surface elements will participate that we are able to draw a straight line between them. These lines should not be disconnected by any other cylinders. Therefore, it is important to examine the possibility of hitting a cylinder by a line and look for the conditions that will lead to this case.

The possibility of intersection of line $\mathbf{q}' = \mathbf{P}' + \mathbf{v}'\,t$, which is a ray between the source and target surface elements located at $\mathbf{p}'$ and $\mathbf{p}''$ respectively, with a cylinder is addressed using Eqs. 3.21, 3.22 and 3.23. To find the intersection points, we need to substitute $\mathbf{q}'$ into the equation of that particular cylinder and solve the leading equation for t, so we get

$$\left(\mathbf{P}' + \mathbf{v}'\,t - \mathbf{P}_b - \left(\mathbf{v} \cdot \left(\mathbf{P}' + \mathbf{v}'\,t - \mathbf{P}_b\right)\right)\vec{v}\right)^2 - r^2 = 0\,. \tag{3.36}$$

Some implementation the equation above can be rewritten in a short format as follows,

$$A\,t^2 + B\,t + C = 0, \tag{3.37}$$

where

$$\begin{aligned} A &= \left\|\mathbf{v}' - \left(\mathbf{v}' \cdot \mathbf{v}\right)\mathbf{v}\right\|^2, \\ B &= 2\left[\left(\mathbf{v}' - \left(\mathbf{v}' \cdot \mathbf{v}\right)\mathbf{v}\right] \cdot \left[\Delta\mathbf{P}_b - \left(\Delta\mathbf{P}_b \cdot \mathbf{v}\right)\mathbf{v}\right], \\ C &= \left\|\Delta\mathbf{P}_b - \left(\Delta\mathbf{P}_b \cdot \mathbf{v}\right)\mathbf{v}\right\|^2 - r^2, \end{aligned} \tag{3.38}$$

where $\Delta\mathbf{P}_b = \mathbf{P}' - \mathbf{P}_b$. So, if value $B^2 - 4\,A\,C$ be greater than (equal to) zero, this equation will have solutions t_1, t_2 (solution t_0), which shows the line and cylinder will intersect. Note that, the cylinder is finite, so the intersection points should be inside the range of the cylinder. Therefore, Eqs. 3.22 and 3.23 need to be satisfied;

$$0 \leq t_i \leq 1\,, \tag{3.39}$$

$$\mathbf{v} \cdot (\mathbf{q}_i - \mathbf{p}_b) > 0\,, \tag{3.40}$$

$$\mathbf{v} \cdot (\mathbf{q}_i - \mathbf{p}_t) < 0\,. \tag{3.41}$$

If the t_i's satisfy these conditions, there exist intersection points, in the range of the finite cylinder. This leads to the neglecting of the contribution of that particular surface element (source) to the configuration form factor fraction calculations.

3.6.3 Caps – Ray Intersection

The analogous procedure should be followed to find any intersection between the straight line and the cylinder caps. For the same line $\mathbf{q}' = \mathbf{P}' + \mathbf{v}'t$, we examine the possibility of intersection with the bottom and top caps. By substituting the line equation inside the caps equations 3.28 and 3.30 we get

$$\mathbf{v} \cdot (\mathbf{P}' + \mathbf{v}'t - \mathbf{P}_b) = 0 \tag{3.42}$$

$$\mathbf{v} \cdot (\mathbf{P}' + \mathbf{v}'t - \mathbf{P}_t) = 0 \tag{3.43}$$

Solving for t we get

$$t_3 = -\frac{\mathbf{v}\cdot\Delta\mathbf{P}_b}{\mathbf{v}\cdot\mathbf{v}'}, \quad \Delta\mathbf{P}_b = \mathbf{P}' - \mathbf{P}_b \tag{3.44}$$

$$t_4 = -\frac{\mathbf{v}\cdot\Delta\mathbf{P}_t}{\mathbf{v}\cdot\mathbf{v}'}, \quad \Delta\mathbf{P}_t = \mathbf{P}' - \mathbf{P}_t \tag{3.45}$$

We note that since these intersection points should be located on the caps, Eqs. 3.29 and 3.31 need to be satisfied as follow:

$$0 \leq t_i \leq 1 \tag{3.46}$$

$$\left(\mathbf{q}_3 - \vec{P}_b\right)^2 < r^2, \quad \text{bottom cap} \tag{3.47}$$

$$\left(\mathbf{q}_4 - \vec{P}_t\right)^2 < r^2, \quad \text{top cap} \tag{3.48}$$

The important point is that if the value $\mathbf{v}\cdot\mathbf{v}'$ at the denominator be equal to zero the line is perpendicular to the cylinder main axis. In this case we need to consider two different scenarios for each cap. If $\mathbf{v}\cdot\Delta\mathbf{P}_i \neq 0$ ($\Delta\mathbf{P}_i = \mathbf{P}' - \mathbf{P}_i$), the line and the caps will not intersect each other. subscript i distinguishes the bottom cap, $i = b$, from the top cap $i = t$. But, if $\mathbf{v}\cdot\Delta\mathbf{P}_i = 0$, it means the line is located on the surface that includes one of the caps. At this situation to check the mutual status of the line and the caps we need to substitute the line equation in the caps equation $(\mathbf{q} - \mathbf{P}_i)^2 = r^2$, it then follows that,

$$(\mathbf{P}' + \mathbf{v}'t - \mathbf{P}_i)^2 = r^2 \tag{3.49}$$

some mathematical implementations simplify it to

$$A't^2 + B't + C' = 0 \tag{3.50}$$

where

$$A' = \mathbf{v}'\cdot\mathbf{v}', \tag{3.51}$$

$$B' = 2\left(\mathbf{v}'\cdot\Delta\mathbf{P}_i\right), \tag{3.52}$$

$$C' = \left(\Delta\mathbf{P}_i\cdot\Delta\mathbf{P}_i\right) - r^2. \tag{3.53}$$

So, if the value $B'^2 - 4\,A'\,C'$ be greater than or equal to zero, there exist intersection point and we need to neglect the contribution of that particular surface element (source) to the geometric configuration factor fraction calculations.

We list the discussions above in follow. A straight line and a cylinder will intersect if and only if they satisfy bellow conditions

- **Finite Cylinder – Ray Intersection**

$$B^2 - 4\,A\,C \geq 0 \tag{3.54}$$

$$t_i \geq 0 \tag{3.55}$$

$$\mathbf{v} \cdot (\mathbf{q}_i - \mathbf{P}_b) > 0 \tag{3.56}$$

$$\mathbf{v} \cdot (\mathbf{q}_i - \mathbf{P}_t) < 0 \tag{3.57}$$

- **Caps-Ray Intersection**

$$\mathbf{v} \cdot \mathbf{v}' \neq 0, \;\; t_i \geq 0, \;\; \Rightarrow \tag{3.58}$$

$$(\mathbf{q}_3 - \mathbf{P}_b)^2 < r^2, \quad \text{bottom cap} \tag{3.59}$$

$$(\mathbf{q}_4 - \mathbf{P}_t)^2 < r^2, \quad \text{top cap} \tag{3.60}$$

$$\mathbf{v} \cdot \mathbf{v}' = 0, \tag{3.61}$$

$$\mathbf{v} \cdot \Delta\mathbf{P}_i = 0, \;\; \Rightarrow \tag{3.62}$$

$$B'^2 - 4\,A'\,C' \geq 0\,. \tag{3.63}$$

3.7 Computational operations optimizing

From previous section, it is clear that in order to calculate the total GCF received by the target cylinder from the other sources (rest of the cylinders) we need to operate a huge amount of computations. A simple calculation shows that for N number of cylinders with M number of mesh grids located on each one, we have $M\,N(M\,N-1)$

different surface elements pair to compute the configuration factor fractions. So, we need to somehow optimize this time consuming procedure. Applying reciprocity relations half of the computational costs are already saved. We continue optimization by decreasing the number of possible pair surface elements which are able to exchange the rays. Earlier, we mentioned the ray which exchanged between source and target should go through a straight line. From this it then follows, A non-zero GCF is computable if and only if surface elements i and j, respectively, located on the cylinders I and II, view each other. More specifically, the only way to draw a straight line, left the i^{th} and hit the j^{th}, is if the surface element i be in front of a plane which is tangent to the cylinder surface includes the target point. The reverse process should meet too. The mutual configuration of surface element i in respect to the cylinder which surface element j is located on, can be listed as follows,

1. **surface elements on the curved surface of two different cylinders**

   Assume the surface elements $(x_i,\, y_i,\, z_i)$ is located on the curved surface of cylinder I. we need first to find the normal $\hat{n}$ at location of the surface elements. Recalling cylinder main axis $\mathbf{v}(a,\, b,\, c)$, we look for $\hat{n} \cdot \mathbf{v} = 0$. Let $\Delta : (x_b + ta,\, y_b + tb,\, z_b + tc)$ be the main parametric line equation of the cylinder along the $\mathbf{v}$. The line passing through $(x_i,\, y_i,\, z_i)$ and intersect with Δ would be of the form $\Delta' : (x_i - x_b - ta,\, y_i - y_b - tb,\, z_i - z_b - tc)$. Since, Δ and Δ' should be normal, applying $\mathbf{v} \cdot \Delta' = 0$ we get

   $$t = (x_i - x_b)\, a + (y_i - y_b)\, b + (z_i - z_b)\, c. \tag{3.64}$$

   Here, we used the fact that $a^2 + b^2 + c^2 = 1$ (i.e. the cylinder main axis is a unit vector). Hence, knowing the t the normal vector direction would be of the form,

   $$\hat{n} : \frac{1}{\lambda}(x_i - x_b - ta,\, y_i - y_b - tb,\, z_i - z_b - tc) = (a',\, b',\, c')\,, \tag{3.65}$$

where λ is the normal coefficient and is of the form,

$$\lambda = \sqrt{(x_i - x_b - ta)^2 + (y_i - y_b - tb)^2 + (z_i - z_b - tc)^2}. \tag{3.66}$$

Therefore, the plane equation tangent to the cylinder at (x_i, y_i, z_i) would be of the form,

$$P_I : a'x + b'y + c'z + d = 0, \tag{3.67}$$

where $d = -a'\,x_i - b'\,y_i - c'\,z_i$. Considering $P_I(\mathbf{x}) = a'x + b'y + c'z + d$, so for point ($x_j$, y_j, z_j) if the value of $P_I(\mathbf{x}_j)$ be greater than one, that point is located in front of the plane. In an analogous manner, the plane equation $P_{II}(\mathbf{x})$ tangent to the cylinder II at (x_j, y_j, z_j) is calculated. So, for point (x_i, y_i, z_i) if the value of $P_{II}(\mathbf{x}_i)$ be greater than one, that point is located in front of the plane. Satisfying these both conditions, it then follows that energy exchanging between them is possible. For any two surface elements which do not satisfy these conditions, further computation is refrained (resulting in $F_{i\to j} = F_{j\to i} = 0$).

2. **Surface element on the Cylinder caps**

For the point (x, y, z) on the caps we realize that the $\hat{n}$ is automatically along the cylinder main axis $\mathbf{v}$. Here, we should note that for the top cap $\hat{n}_t = \mathbf{v}$, but for the bottom cap $\hat{n}_b = -\mathbf{v}$. So, the equations of the top and bottom caps can be expressed as follows,

$$P_b : -ax - by - cz + d_b = 0\,, \tag{3.68}$$

$$P_t : ax + by + cz + d_t = 0\,, \tag{3.69}$$

where

$$d_b = ax + by + cz\,, \tag{3.70}$$

$$d_t = -ax - by - cz\,. \tag{3.71}$$

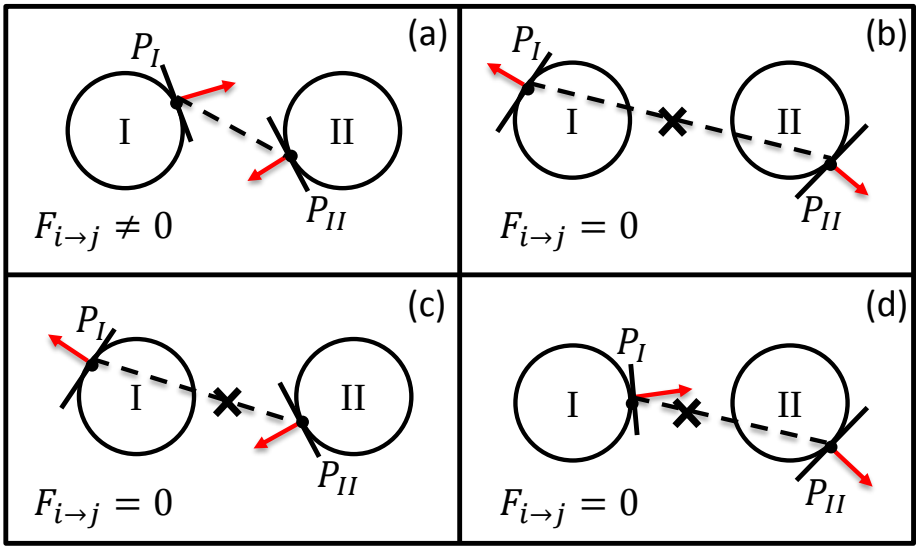

Figure 3.10: (Color online) Two-dimensional schematic illustration of optimization procedure. Panel (a) the only case which will remain in GCF calculation. All other cases, panels (b), (c) and (d), are refrained of further computation since the energy exchange between two surface areas is forbidden.

So, for any point located at $\mathbf{x}(x, y, z)$ if either $P_b(\mathbf{x})$ or $P_t(\mathbf{x}) > 0$, the point is in front of the plane and exchanging of the rays between them is possible. For any point which not satisfies these conditions, they are located behind the plane and are out of GCF calculation procedure.

The procedure demonstrated above is schematically depicted in Fig. 3.10, where a 2D illustration of different possible cases has been drawn.

3.8 Results and discussion

So far the model required for thermal regime analysis has been constructed. The FiberForm® has been simulated using artificial non-overlapped perfect cylinders with arbitrary size and orientation (see Fig. 3.4). In following discussion the radiative properties such as conductivity of the simulated FiberForm® is determined. The calculated conductivity values are also used in the continuum heat equation, and the results are compared to the ones obtained using the direct simulation approach.

3.8.1 Effective conductivity

To calculate the elements of the conductivity matrix in Eq. (2.36) we act as follows. Temperature gradient along one axis is imposed. Suppose the x-axis is used, then Temperature gradient along y and z axis, $\partial T/\partial y = 0$ and $\partial T/\partial z = 0$, respectively, then Eq. (2.35) can be rewritten in the form of:

$$q_x = -\kappa_{x\,x}\,\frac{\partial T}{\partial x}\,, \tag{3.72}$$

$$q_y = -\kappa_{y\,x}\,\frac{\partial T}{\partial x}\,, \tag{3.73}$$

$$q_z = -\kappa_{z\,x}\,\frac{\partial T}{\partial x}\,. \tag{3.74}$$

Thus, determining $\kappa_{x\,x}$, $\kappa_{y\,x}$, and $\kappa_{z\,x}$ is just depending on the predefined temperature gradient along the x-axis. In an analogous manner for each axis three conductivity matrix elements can be readily determined.

The above procedure is carried out as follows. For specified values of temperature T, a temperature gradient is systematically applied along each axis. This gradient is applied such that a 1 K difference of temperature assure the accurate dependency on temperature. For instance, the $\kappa_{x\,x}$, $\kappa_{y\,x}$, and $\kappa_{z\,x}$ at a temperature of 3000 K, are determined using a linear variation of temperature, along the x-axis through the whole fiducial volume, ranging from 2999.5 K to 3000.5. This process is then repeated for $T \in [0, 6000]$ K. An adiabatic boundary condition is imposed by forcing a null heat flux on each imaginary wall, as illustrated in Fig. 2.3.

The results of this analysis are plotted as a function of T in Fig. 3.11. From the figure, a minimum effective conductivity along the z-direction, among main axes, is clear. This was already predicted since the fibers are distributed inhomogeneously (see Fig. 3.4), as well are oriented within a $\pm 15.0°$ bias from the xy-plane. The temperature averaged values of the heat conductivity elements are printed in Table

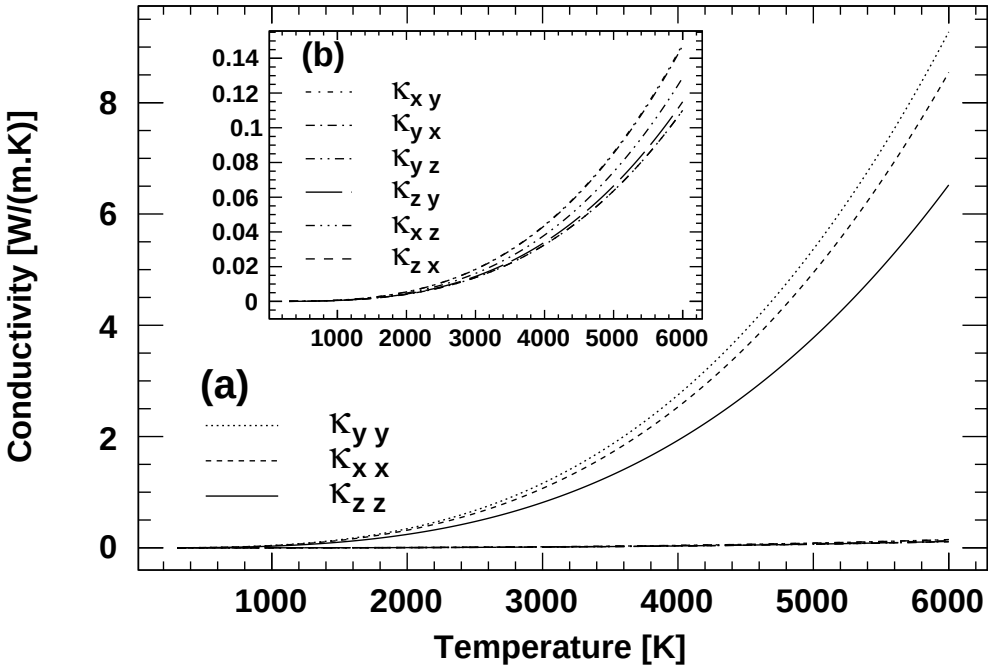

Figure 3.11: Effective conductivity matrix elements $\kappa_{m\,n}$ as a function of temperature are shown in panel (a). The small values of the conductivity matrix elements are zoomed in panel (b).

3.1(a). The averaged definition is defined as follows,

$$\langle \kappa_{m\,n} \rangle_T = \frac{1}{T_{\text{final}} - T_{\text{initial}}} \int_{T_{\text{initial}}}^{T_{\text{final}}} \kappa_{m\,n} dT. \tag{3.75}$$

The Table 3.1(a) implies an orthotropic behavior of the material since the diagonal terms are much greater than the others, $\kappa_{m\,n} \ll \kappa_{m\,m}$ (see also Ref. [81]).

The polynomial dependency on temperature in Fig. 3.11 assures the results agreement with Rosseland hypothesis defined in Ref. [61], where a cubic dependence to the temperature is expected. From the Rosseland radiation model, the radiative heat flux $\vec{q}_r$ has the same form as the Fourier conduction law,

$$\vec{q}_r = -K \epsilon \sigma T^3 \vec{\nabla} T. \tag{3.76}$$

Table 3.1: (a) Temperature averaged effective radiative, (b) Geometric factor reconstructed from Rosseland model, (c) Temperature averaged effective radiative conductivity along the principal axis, and (d) Geometric factor reconstructed from Rosseland model along the principal axis.

(a)	$\langle\kappa\rangle_T$ [W/(m K)]			(b)	K [10^{-4} m]		
	$\boldsymbol{x}$	$\boldsymbol{y}$	$\boldsymbol{z}$		$\boldsymbol{x}$	$\boldsymbol{y}$	$\boldsymbol{z}$
$\boldsymbol{x}$	2.249	0.039	0.029	$\boldsymbol{x}$	8.210	0.142	0.106
$\boldsymbol{y}$	0.039	2.441	0.032	$\boldsymbol{y}$	0.142	8.910	0.117
$\boldsymbol{z}$	0.029	0.032	1.717	$\boldsymbol{z}$	0.106	0.117	6.266

(c)	$\langle\lambda\rangle_T$ [W/(m K)]			(d)	Λ [10^{-4} m]		
	1	**2**	**3**		**1**	**2**	**3**
	2.450	2.242	1.714		8.186	8.944	6.256

and in a matrix form like Eq. 2.36,

$$\begin{pmatrix} q_{r,x} \\ q_{r,y} \\ q_{r,z} \end{pmatrix} = -\epsilon\sigma T^3 \begin{pmatrix} K_{x\,x} & K_{x\,y} & K_{x\,z} \\ K_{y\,x} & K_{y\,y} & K_{y\,z} \\ K_{z\,x} & K_{z\,y} & K_{z\,z} \end{pmatrix} \begin{pmatrix} \frac{\partial T}{\partial x} \\ \frac{\partial T}{\partial y} \\ \frac{\partial T}{\partial z} \end{pmatrix}. \tag{3.77}$$

Therefore, the data can be fitted to a cubic function of the form

$$\kappa_{m\,n} = K_{m\,n}\epsilon\sigma T^3, \tag{3.78}$$

where K_{mn} is a geometric factor. Finding fit parameters K_{mn} leads to the K-factor matrix elements listed in Table 3.1(b). From the matrix theory the effective radiative conductivity tensor possesses three mutually orthogonal principal axes (i.e. the orientation of the geometry where the off-diagonal terms are zero) which are associated with three real eigenvalues. These eigenvalues are listed in Table 3.1(c) and (d) regarding to panels (a) and (b), respectively. The following points are important to discuss. First, comparison between the orthogonal values and the diagonal elements shows that the geometry was already well oriented along the main axes. Also, $\kappa_{xx} \approx \kappa_{yy}$ (in-plane (IP) directions), and are different from κ_{zz} (the through-the-thickness (TTT) direction), which is a consequence of the fact that the cylindrical fibers were oriented within a $\pm 15.0^\circ$ bias from the xy-plane.

3.8.2 Transient thermal conduction analysis

Following the discussion in section 2.8, the calculated net heat transfer q_i is applied to determine the new surface temperature T_i at time step Δt using the following equation,

$$T_k^{(\tau+1)} = \frac{q_k^{(\tau)} A_k \Delta t}{V_k \rho_c c_p} + T_k^{(\tau)}, \tag{3.79}$$

where ρ, V, and c_p are the density, volume, and specific heat capacity of the fibers. The temperature is assumed to be uniformly distributed on the surface of the fiber. Superscripts in parenthesis denote iteration counters (i.e. updated value $\tau + 1$ and old value τ).

Since Eq. (3.79) is a discrete version of the heat equation and is, therefore, influenced by the choice of Δt, a convergence study was carried out to ensure that no numerical error was generated. The value of $\Delta t = 0.1$ µs was determined to be small enough to generate an average root-mean-square error on the temperature of less than 10^{-9} when compared to a time step twice as large.

A transient heat transfer analysis of the fibrous volume is performed, using the DS method combined with Eq. (3.79). The emissivity, specific heat capacity, and density of the fibers are taken to be $\epsilon = 0.85$, $c_p = 1000.0$ J/(kg K), and $\rho_c = 1800.0$ kg/m^3, respectively. These values are representative of literature data for carbon preform [64].

As initial condition, all fibers have a temperature of 300 K, less a small group (slice) of fibers located near the $z = 0.5$ mm boundary, within a $\Delta z = 0.02$ mm distance. This group of fibers are instead initialized at 3000.0 K. Applying the energy exchange process (discussed in Section 3.2) to the entire fiducial volume, the new temperature of the fibers is calculated using Eq. (3.79). Updated values of T_k are retained, and the new radiosities $q_{\text{out},\,k}$ are determined by solving the system of linear Eqs. (2.32). This process is then repeated a number of times until the values of all the

T_k do not change appreciably between successive sweeps (less than 0.1 K throughout the volume), thereby implying that the iteration process has converged. In this simulation, an adiabatic boundary condition is imposed by applying the symmetry condition on all walls.

The goal of the present method is to obtain values for the effective conductivity that are linked to a specific fiber-scale geometry but can be used in a macro-scale simulation. Thus, the results from the approach developed above (DS at fiber scale) are compared to results obtained from the heat conduction model, derived from Fourier's law and from the conservation of energy. The solution of this second model, called Finite Difference (FD), is obtained by numerically solving the one-dimensional transient heat equation:

$$\rho c_p \frac{\partial T}{\partial t} = \frac{\partial}{\partial z}\left[\kappa_{z\,z}(T)\frac{\partial T}{\partial z}\right],$$

where effective density $\rho = \rho_c(1-\phi) = 360.0$ kg/m^3, $c_p = 1000.0$ J/(kg K), and $\kappa_{z\,z}(T) = \epsilon\sigma K_{zz} T^3$. The equation is solved over a 1.0 mm domain with the first $\Delta z = 0.02$ mm initially at 3000.0 K and the rest at 300.0 K. Both boundaries of the domain are considered adiabatic.

Temperatures for three different locations: $z = -0.25$ mm, $z = 0.0$, and $z = 0.25$ mm, are extracted for each of these models. For the DS model, the temperatures for specified locations are considered to be the average temperature of a group of fibers located within $z \pm \Delta z$ ($\Delta z = 0.01$ mm) domain, which corresponds to the heat conduction along the z-axis. Temperature evolution curves are shown in Fig. 3.12 where there is good agreement between both models. The shaded color bands correspond to the standard error of the mean of the temperatures as calculated by the DS model.

The discrepancy in Fig. 3.12, even if considered minimal, is a consequence of multiple approximations. First, although the DS model is considered to be an accurate representation of the heat transfer phenomena, the conversion of the heat to temperature (Eq. (3.79)) is a gross approximation since the fibers are assumed to have a

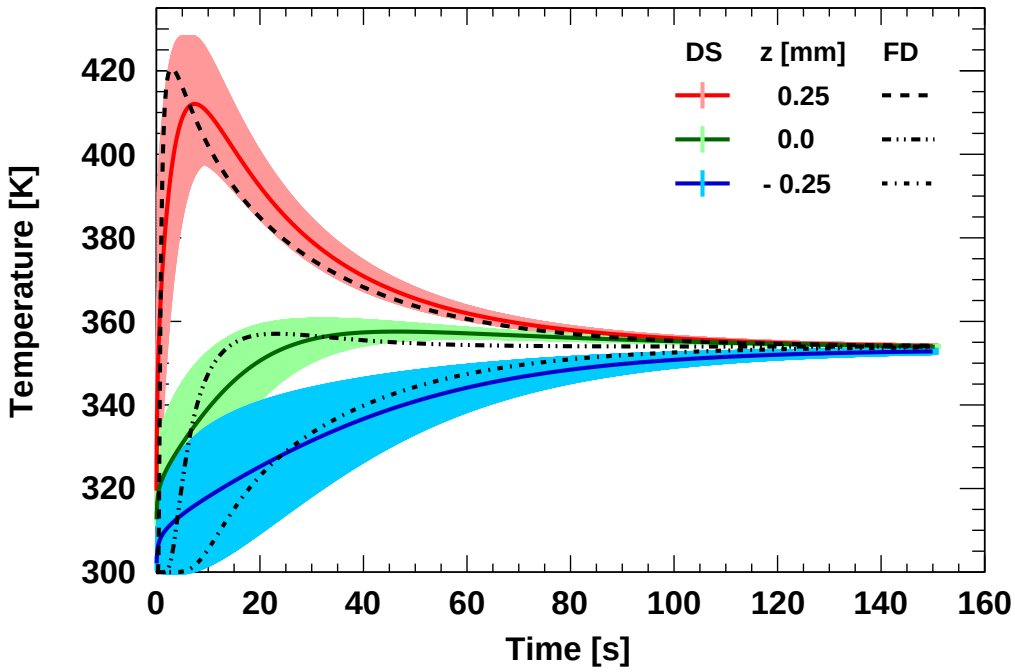

Figure 3.12: (Color online) Comparison of the temperature evolution of the thermal radiant regime between the Direct Simulation (DS) and the Finite Difference (FD) models at discretized z positions. The standard error of the mean of the temperatures calculated from the DS model for each $z = -0.25$ mm, 0.0 mm, and 0.25 mm are shown with shaded color bands in blue, green, and red respectively.

uniform temperature. Therefore, even though the evaluation of the κ matrix is considered to be highly accurate, the transient heat transfer analysis of the DS approach is not. Another source of discrepancy comes from the fact that the DS model is three-dimensional simulation, but the volume-averaged numerical calculation is only in one dimension since all cross terms of the effective radiative conductivity matrix are neglected.

3.9 Remarks

A three-dimensions direct simulation model was developed to determine the effective radiative conductivity within a fiducial volume filled with randomly sized, positioned, and oriented cylindrical fibers. Anisotropic behavior of the fibrous model was high-

lighted by calculating the effective radiative conductivity matrix for a representative geometry. This conductivity was shown to be a function of both temperature and the orientation of the fibers. The effective conductivity was used in a transient volume averaged heat equation and compared to the direct simulation approach. The results showed accurate agreement that validated the approach. The methodology developed and presented here could be use to obtain accurate values of the effective conductivity of realistic three-dimensional material geometry, such as the ones obtained from computed X-ray micro-tomography [64]. These values could then be used in volume-averaged material response code [84, 85] to increase the fidelity in heat transfer analysis. Moreover, performing such an analysis on a real material would allow to compare to experimental analysis.

Chapter 4

FiberForm® simulation using real geometry

In the previous chapter, a simplified three-dimensional direct simulation model was developed. The model was used to study the effective radiative conductivity of fibrous material using an artificial geometry with properties resembling those of carbon-preform. Simulations were carried out using artificial non-overlapped perfect cylinders with arbitrary size and orientation which were irregularly positioned within a cubic enclosure. This ultimately resulted in a heterogeneous distribution of the cylinders, resembling anisotropic properties of the FiberForm®. It was shown that the effective radiative conductivity is a function of both temperature and the orientation of the fibers.

In this chapter, instead of employing perfect cylinders, we now take advantage of an available three-dimensional micro-tomography image to achieve a better understanding of the properties of the fiber-preforms at the microscopic scale. This is achieved by using the real architectures extracted from computed micro-tomography to understand and model the energy-exchange process of the fibrous material. For that purpose, a 3D reconstructed geometry is implemented in a robust GCF calculator

algorithm. The results are retained and implemented in a systematic radiative transient regime model to study the radiative conductivity properties of the FiberForm®. FiberForm® is a carbon fiber insulator that serves as the preform to certain TPS materials [88]. To demonstrate the validity of the approach, the radiative conductivity tensor of the sample is calculated, and compared to experimental results.

4.1 Test geometry

Using X-ray computed tomography a triangulated polygon surface mesh of fibrous material was generated to characterize the microstructural properties of FiberForm®. The image analysis were caried out at the Advanced Light Source (ALS) at Lawrence Berkeley National Laboratory [89]. High resolution (low noise) data obtained from ALS makes X-ray tomography technique a potentially valuable tool in porous substrates studies. The polygon surface mesh has been visualized via Wolfram Mathematica software, and illustrated in Fig. 4.1. The data set is a collection of 168,804 vertices which ultimately construct $M = 56{,}268$ triangle faces (solid opaque surfaces) defining the external shape of fibrous material in 3D. The triangles are identified by set of vertices $\{(\mathbf{V}_{1,k}\ , \mathbf{V}_{2,k}\ , \mathbf{V}_{3,k})\}$, normal directions $\{\mathbf{n}_k\}$ and centroids coordinate $\{\mathbf{C}_k\} = \{(\,C_{x,k}\ , C_{y,k}\ , C_{z,k}\,)\}$. Subscript k refers to k^{th} triangular face. The coordinates of the centroid is calculated by averaging the x, y and z component of the vertices (e.g. $C_x = \frac{1}{3}(V_{1,x} + V_{2,x} + V_{3,x})$). A relative configuration of two triangular mesh grids is illustrated schematically in Fig. 4.2.

To ensure that all radiative contributions are accounted for, the visualized FiberForm® is enclosed by a cubic fiducial volume (see Fig. 4.3a) whose boundary walls are composed of the same material as the fibrous material (diffuse and gray). Also, the surfaces of the enclosure are taken to be perfectly insulated from external heat addition or removal. Another assumption in the present analysis is that each separate surface of the enclosure is taken to be isothermal. However, if the bound-

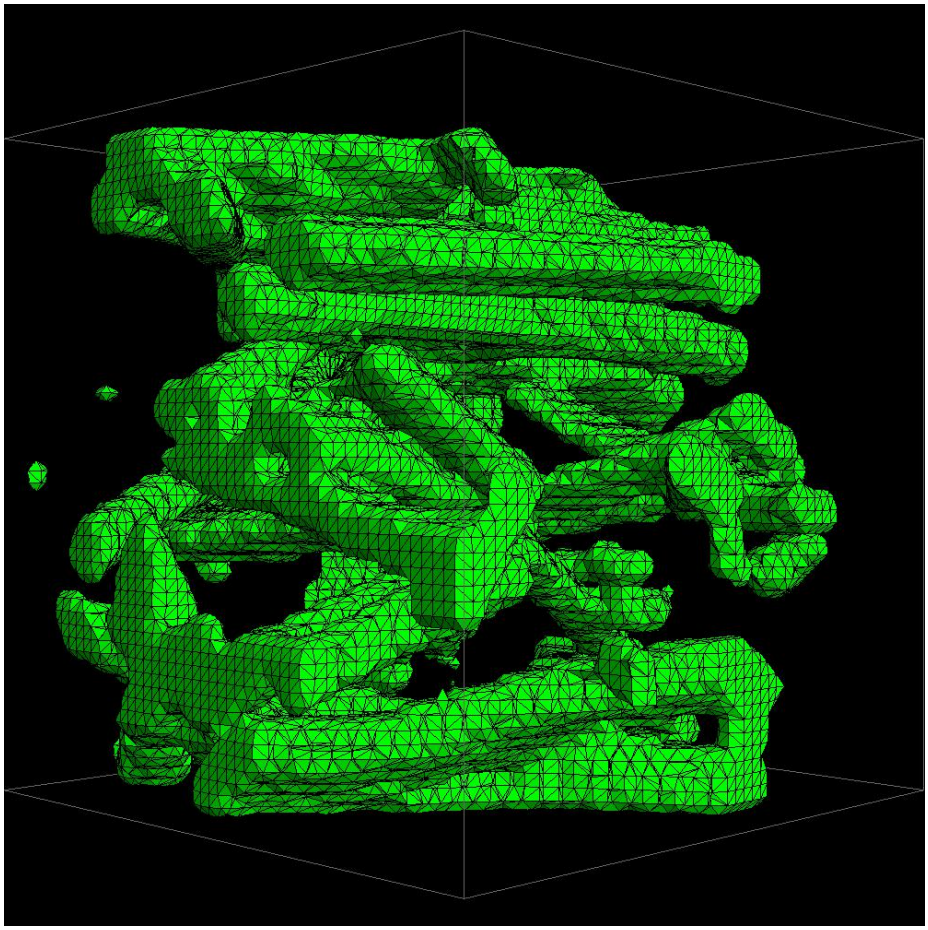

Figure 4.1: (Color online) Schematic illustration of three-dimensional microscopic scale of FiberForm® real geometry extracted from computed tomography.

ary conditions imposed to the analysis are such that the temperature needs to vary markedly over an area, the area can be readily subdivided into smaller isothermal portions.

4.2 GCF calculation and analysis

The GCF calculation is an important aspect in determining the radiation interchange between surface elements in heat transfer. The computation of GCF involves integrating over the solid angles subtended by each surface segments, if surfaces have common view field. In the absence of an exact analytical expression for GCF, tedious numerical integration is required. Moreover, so many areas (N = six internal enclosure sides

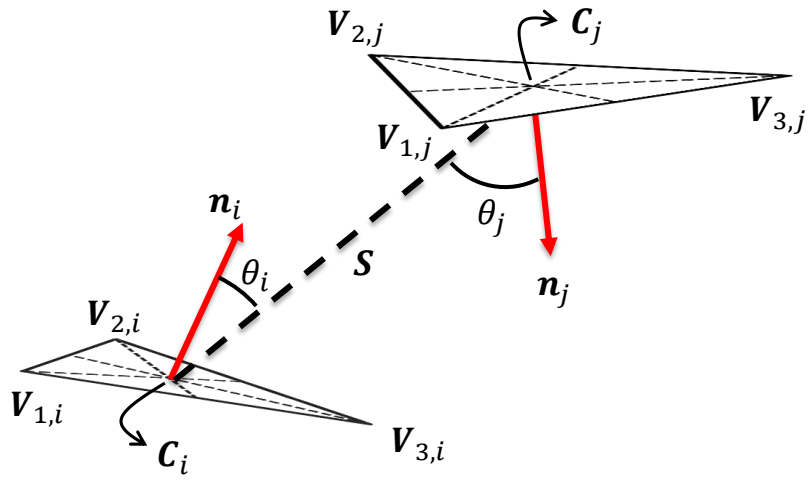

Figure 4.2: (Color online) Schematic configuration of the i^{th} and j^{th} triangular mesh extracted from computed tomography.

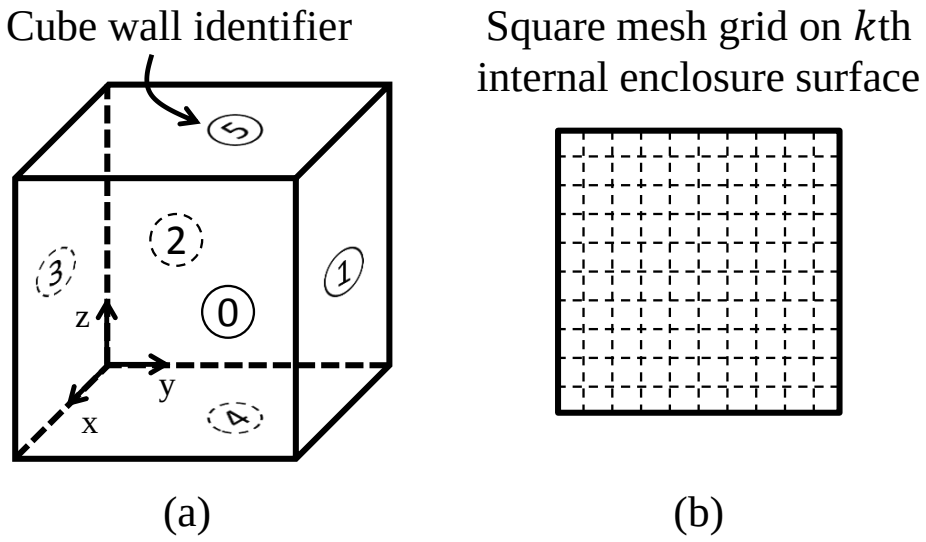

Figure 4.3: Panel (a): Schematic figure of the specific experimental geometry employed in the model. A cubic enclosure with, 0.1 mm (L_x) $\times$ 0.1 mm (L_y) $\times$ 0.1 mm (L_z), which contains the fibrous material. Panel (b): Dense square mesh grid superposed on the internal enclosure surfaces of area A.

+ M triangular mesh grids) require excessive computation time. Hence, a robust algorithm with fast implementation is essential to reduce computational complexity. Mathematical details and general formulas for the GCF numerical calculation were explained and verified in chapter 2. Here, for the sake of completeness, a step-by-step set of operations for GCF calculation performance is presented. Also, as an aid to

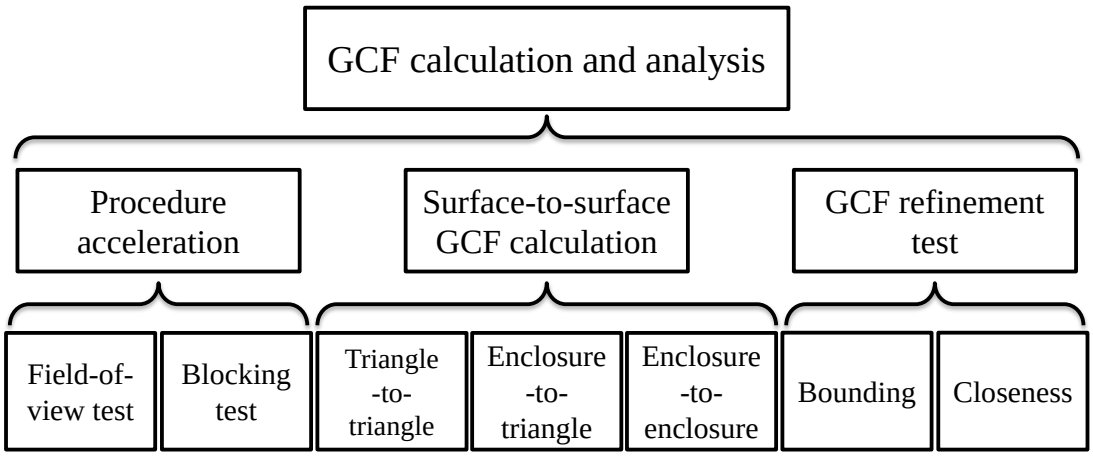

Figure 4.4: Algorithm flowchart of geometric configuration factor calculation.

the interested reader, a set of filters deployed on the algorithm in order to streamline the computations are disclosed. Each of the above is written in C++ and executed on University of Kentucky High Performance Computing (HPC) hardware [90]. A summary of geometric configuration factor calculation and analysis demonstrated in this section is schematically depicted in Fig. 4.4.

4.2.1 Triangle - Triangle GCF calculation

Set of triangular areas reconstructed from computed tomography is considered to include tiny surface elements (isothermal, opaque, and diffuse) defined as $\{a_k\}$. Then, it follows that the fraction of energy leaving a_i that is incident on the second surface a_j is denoted by $F_{a_i \to a_j}$. In general, such a factor is given by,

$$F_{a_i \to a_j} = \frac{\cos\theta_i \, \cos\theta_j}{\pi \, S_{ij}^2} \, a_j \ , \tag{4.1}$$

where, θ $(0 \leq \theta_i \, , \, \theta_j \leq \pi/2 \,)$ is the angle between the normal of the surface elements and the line of length S joining the triangles centroid (see Fig. 4.2). To minimize the computational cost, a reciprocal equation which determines $F_{a_j \to a_i}$ with less computational effort is deployed. The reciprocity relation is of the form,

$$a_i \, F_{a_i \to a_j} = a_j \, F_{a_j \to a_i} \ . \tag{4.2}$$

4.2.2 Internal enclosure surface - Triangle GCF calculation

GCF calculation between the finite area internal enclosure surfaces and predefined triangular surface elements is addressed. To accomplish the numerical integration, a dense square mesh grid set $\{\mathrm{d}A\}$ is superposed on each of the internal enclosure surfaces of area A (see Fig. 4.3b). Then, the configuration factor from each small triangular surface area a_i to the finite receiving area A_j is given by,

$$F_{a_i \to A_j} = \int \frac{\cos\theta_i \, \cos\theta_k}{\pi \, S_{i\,k}^2} \, \mathrm{d}A \; , \tag{4.3}$$

which in a discretized form it can be rewritten in the form of

$$F_{a_i \to A_j} = \frac{\Delta A}{\pi} \sum_k \frac{\cos\theta_i \cos\theta_k}{S_{ik}^2}, \tag{4.4}$$

where subscripts i, j and k refer to i^{th} triangular surface area, j^{th} internal enclosure surface and k^{th} subsurface, respectively. The numerical results are mesh independent, using a surface discretization where each subsurface is smaller than the total area of the internal enclosure side by 4 orders of magnitude. Again, a reciprocity relation would be vital to accelerate the algorithm performance. The equation would be of the form,

$$a_i \, F_{a_i \to A_j} = A_j \, F_{A_j \to a_i} \; . \tag{4.5}$$

4.2.3 Internal enclosure surface - Internal enclosure surface GCF calculation

Finally, for the case of radiation leaving internal enclosure surface A_i and reaching another internal enclosure surface A_j, the GCF expression would be of the form,

$$F_{A_i \to A_j} = \frac{1}{A_i} \int\int \frac{\cos\theta_k \, \cos\theta_\ell}{\pi \, S_{k\,\ell}^2} \, \mathrm{d}A \, \mathrm{d}A \; , \tag{4.6}$$

which in a discretized form it can be rewritten in the form of,

$$F_{A_i \to A_j} = \frac{(\Delta A)^2}{\pi A_i} \sum_{k,\ell} \frac{\cos\theta_k \cos\theta_\ell}{S_{k\ell}^2}. \tag{4.7}$$

Table 4.1: Summary of geometric configuration factor and reciprocity relation.

Case	Geometric configuration factor	Reciprocity
1	$F_{a_i \to a_j} = \frac{\cos\theta_i \cos\theta_j}{\pi S_{ij}^2} a_j$	$a_i F_{a_i \to a_j} = a_j F_{a_j \to a_i}$
2	$F_{a_i \to A_j} = \frac{\Delta A}{\pi} \sum_k \frac{\cos\theta_i \cos\theta_k}{S_{ik}^2}$	$a_i F_{a_i \to A_j} = A_j F_{A_j \to a_i}$
3	$F_{A_i \to A_j} = \frac{(\Delta A)^2}{\pi A_i} \sum_{k,\ell} \frac{\cos\theta_k \cos\theta_\ell}{S_{k\ell}^2}$	$A_i F_{A_i \to A_j} = A_j F_{A_j \to A_i}$

Subscripts k and ℓ refer to k^{th} and ℓ^{th} subsurfaces on i^{th} and j^{th} internal enclosure surfaces, respectively. Here, the associated reciprocity relation is given by,

$$A_i \, F_{A_i \to A_j} = A_j \, F_{A_j \to A_i} \, . \tag{4.8}$$

For the sake of simplicity, the relations demonstrated in sections 4.2.1, 4.2.2 and 4.2.3, are listed in Table 4.1.

4.2.4 Acceleration of the GCF calculation

In general, for N (predefined) surface areas $N(N-1)$ geometric configuration factors ($\sim 3 \times 10^9$) need to be calculated. Applying reciprocity relation Eqs. (4.2), (4.5) and (4.8) half of the computational costs are already saved. Even so, the quantity of triangulated polygon surface areas from computed tomography and the dense square mesh grid on the internal enclosure surfaces keep the GCF calculation very intensive. Geometric properties of surface segments are used to reduce the CPU-time cost.

GCF Field-of-view test

A non-zero GCF is computable if and only if surfaces i and j view each other. More specifically, each surface area is assumed to be surrounded by a hemisphere of infinite radius, and subtends a solid angle of 2π steradians about the predefined centroid of its base and in the direction of its associated surface normal. Under these circumstances, surfaces i and j are able to exchange radiation if and only if two domes,

either fully or partially, faced each other. In order to mathematically implement this filter, following discussion is proposed. Given centroids and normal vectors associated to the i^{th} and j^{th} surface areas, infinite planes $P_i\,(x,\,y,\,z)$ and $P_j\,(x,\,y,\,z)$ are constructed. Therefore, the viewability condition would be a true statement if and only if both $P_i\,(\mathbf{C}_j)$ and $P_j\,(\mathbf{C}_i)$ are positive values. As discussed above, this is ultimately equivalent with a constraint on the relative orientation of two surface segments with respect to their associated normal directions (i.e. $\cos\theta_i$ and $\cos\theta_j > 0$). otherwise, further computation is refrained (resulting in $F_{i\to j} = F_{j\to i} = 0$).

GCF Obstruction test

Even if surfaces i and j pass the first filter, they are just candidates for radiation exchange. They need to pass another filter to ensure that the radiation exchange has occurred. In case of an isotropic emission (diffuse-gray approximation), radiation exchange between two sources is possible, if and only if their line-of-sight (LoS) is not blocked by an opaque object. To address this, uniform radiation is characterized by a set of straight lines rising from the source, diffusing in all directions and reaching the target. Therefore, the energy exchange would be prevented, if an opaque object (i.e. one of the triangular mesh grids) intersects the straight path from centroid i to centroid j. Second filter would be examined over all the triangular mesh grids and save CPU-time significantly by preventing any further computation once the condition statement becomes true (resulted in $F_{i\to j} = F_{j\to i} = 0$).

Finding surface segments which are incapable of radiation interchange, the filters play an essential role to achieve a more realistic heat transfer model. The algorithm associated with above can be readily designed using simple algebraic implementation. It is also worth noting that, second filter does not necessarily assure a fully blocked radiation. In fact, in some cases (based on the triangles' size and orientation) energy can be partially exchanged, since portions of surfaces can still view each other. To

achieve a better resolution, the triangles computed from micro-tomography can be subdivided into smaller triangular portions. An engineering judgment is required to define a "figure of merit" for the selection of an optimal number of subsurface area elements. This can be supplemented with following discussion.

GCF algebraic test

Details of our GCF algebra are as follows:

1. Bounding: GCF's are bounded to $0 \leq F_{i \to j} \leq 1$ (i.e. the GCF $F_{i \to j}$ is the fraction of energy exiting surface element i, that impinges on surface element j). Bounding is the evaluation criteria of resolution which should have been met, by triangular mesh grid computed from micro-tomography, prior to GCF calculation. Such that, if bounding between i^{th} and j^{th} triangular elements was violated, those triangles should be subdivided into smaller triangular portions. In a complex scene, there can be any number of triangles, which can be divided into even more surface segments. To address this, from Eq. (4.1) it is clear that the term $\cos\theta_i \, \cos\theta_j \, / \, \pi$ is always < 1, hence decent resolution would be achieved if condition $a_j \, / \, S_{ij}^2 \leq 1$ is satisfied over all the triangles.

2. Closeness: Summing up all GCF's from a given surface in an enclosure must equal 1 ($\sum_j F_{i \to j} = 1$). But, due to the numerical errors associated with the size of the discretized surface segments, the summation is slightly smaller than one ($1 - \xi$, where $\bar{\xi} \sim 10^{-3}$). In order to compensate that, a weight based distribution algorithm is applied to distribute ξ among the configuration factors such that the summation leads to 1.

A bin-averaged "3D map" of calculated bilateral GCF's is shown in Fig. 4.5. Each bin-averaged is calculated as the average of the F_{ij} values lying in 562×562 consecutive interval of (i, j) combinations. For instance, F_{ij} values for $(i, j) = (0, 0) \to (561, 561)$

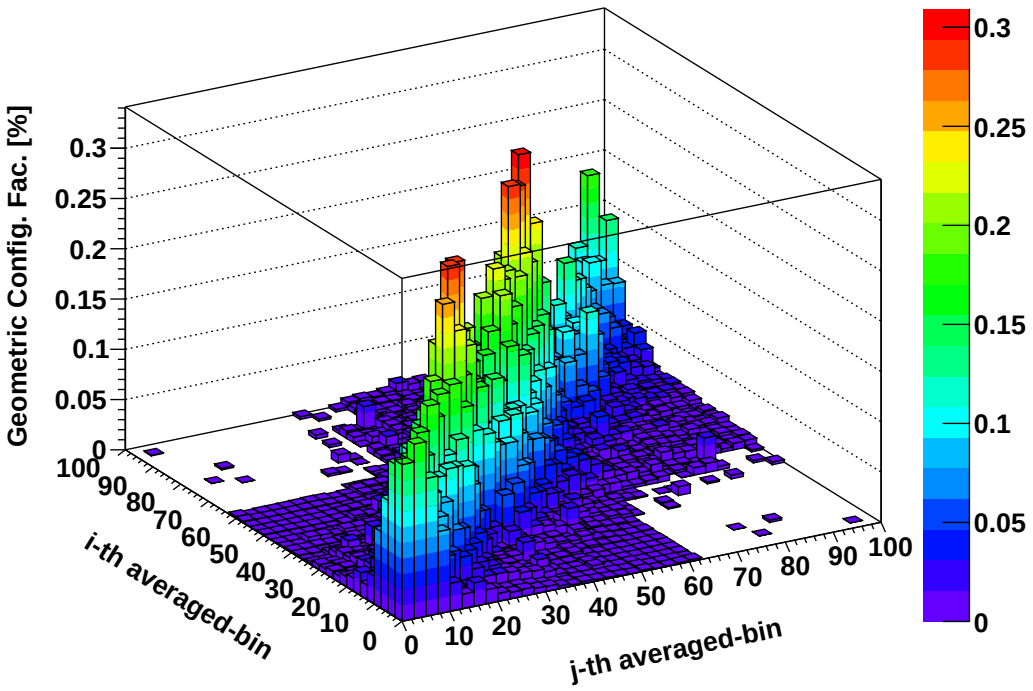

Figure 4.5: (Color online) Calculated geometric configuration factors have been plotted in a bin-averaged over 562×562 consecutive (i, j) combinations.

are averaged. This mean value is assigned to the bin $(0, 0)$ of Fig. 4.5. In the same way, the F_{ij} values for $(i, j) = (562, 0) \rightarrow (1123, 561)$ are averaged and mapped to bin $(1, 0)$, and so on. So, the radiative properties – such as conductivity κ [W m^{-1} K^{-1}] – are expected to show directional dependence. Therefore, the matrix form of the law of heat conduction (Fourier's law) for such an anisotropic fibrous medium can be written as,

$$\begin{pmatrix} q_x \\ q_y \\ q_z \end{pmatrix} = - \begin{pmatrix} \kappa_{x\,x} & \kappa_{x\,y} & \kappa_{x\,z} \\ \kappa_{y\,x} & \kappa_{y\,y} & \kappa_{y\,z} \\ \kappa_{z\,x} & \kappa_{z\,y} & \kappa_{z\,z} \end{pmatrix} \begin{pmatrix} \partial_x T \\ \partial_y T \\ \partial_z T \end{pmatrix} . \tag{4.9}$$

∂_i denotes gradient operator in Cartesian coordinates (i.e. ∂/∂_x, ∂/∂_y and ∂/∂_z), and the diagonal elements $\kappa_{i\,i}$ are radiative conductivity along the main axes.

4.3 Radiation exchange model

As discussed earlier in 2.8, for the i^{th} surface segment, radiosity $q_{\text{out},\,i}$ [W m^{-2}] is composed of emitted irradiance derived from the Stefan-Boltzmann law plus reflected irradiance derived from incident radiation $q_{\text{inc},\,i}$ [W m^{-2}]. Therefore, in a diffuse-gray approximation, where absorptivity and emissivity (ϵ) coefficients are equal and depend only on temperature T_i, the balance equation between $q_{\text{out},\,i}$ and $q_{\text{inc},\,i}$ is given by

$$q_{\text{out},\,i} = \epsilon\sigma T_i^4 + (1-\epsilon)\, q_{\text{inc},\,i}\ . \tag{4.10}$$

σ denotes the Stefan-Boltzmann constant [W m^{-2} K^{-4}]. For an enclosure which is composed of 6 internal boundaries and contains M small surface segments, Eq. (4.10) becomes more complicated. A complex radiative exchange occurs as radiation leaves a surface, travels through the enclosure, reflects from segments and reaches other surfaces. For a N-body problem like above, $q_{\text{inc},\,i}$ is determined by summing over the portions of the radiation leaving the segments within the fiducial volume that arrive at the i^{th} surface. Applying some mathematic implementations (discussed in 2.8), Eq. (4.10) in a comprehensive form can be generalized as follows,

$$q_{\text{out},\,i} - (1-\epsilon)\sum_{j=0}^{N-1} F_{i\,j}\, q_{\text{out},\,j} = \epsilon\sigma T_i^4\,, \quad i \in \{6,\,\ldots\,,N-1\}\,. \tag{4.11}$$

Also, in place of the enclosure boundaries, which are assumed to be perfectly insulated, a symmetric condition ($q_{\text{inc}} = q_{\text{out}}$) is imposed such that Eq. (4.11) can be rewritten as

$$q_{\text{out},\,i} - \sum_{j=0}^{N-1} F_{i\,j}\, q_{\text{out},\,j} = 0\,, \qquad i \in \{0,\,1,\,2,\,3,\,4,\,5\}\,. \tag{4.12}$$

Eq. (4.11) plus Eq. (4.12) generate N linear equations with N unknown radiosities $\{q_{\text{out},\,i}\}_{i=0}^{N-1}$ and N known temperatures $\{T_i\}_{i=0}^{N-1}$. So, a $N \times N$ system of linear equations is constructed and can be readily solved via standard numerical methods (e.g.,

Gaussian elimination). It then follows that, the incident radiation set $\{q_{\text{inc},\,i}\}_{i=0}^{N-1}$, can be calculated by

$$q_{\text{inc},\,i} = \sum_{j=0}^{N-1} F_{i\,j}\, q_{\text{out},\,j}\ . \tag{4.13}$$

4.4 Results and discussion

The nine elements of the effective conductivity matrix presented in Eq. (4.9) are determined in a systematic procedure as follows. First, a temperature difference ΔT is imposed between two enclosure walls (called here T_I and $T_I I$) normal to the i-axis ($i \in \{x,\, y,\, z\}$), while the symmetric condition is imposed for the enclosure walls normal to the j-axis ($j \neq i$ and $\in \{x,\, y,\, z\}$). Then, a linear temperature gradient $\partial_i T$ ranging from T_{II} to T_I ($T_{II} > T_I$) is applied along i-axis, such that the k^{th} triangular mesh grid is assigned temperature

$$T_k = T_{II} - \Delta T \frac{C_{i,k}}{L_i}. \tag{4.14}$$

$C_{i,\,k}$ and L_i are previously defined as i-component of k^{th} triangular centroid coordinate and the enclosure volume dimension, respectively. The temperature variation imposed on the domain in the i-direction ultimately leads to $\partial_{j\neq i} T = 0$. Therefore, from Eq. (4.9) it then follows that, for each i-axis three conductivity elements $\kappa_{x\,i}$, $\kappa_{y\,i}$, and $\kappa_{z\,i}$ at a given mean temperature of $T = \frac{1}{2}(T_I + T_{II})$ can be readily determined. From the Rosseland model [61] it is also well established that, the radiative conductivity is expected to exhibit a "cubic polynomials" dependence on temperature. Therefore, the radiative conductivity matrix elements can be fitted to a third order polynomial of temperature. The foregoing discussion can be summarized in the following set of equations,

$$\kappa_{ji}\,(T) = -\,q_j \frac{L_i}{\Delta T} = K_{ji}\,\epsilon\,\sigma\,T^3 \tag{4.15}$$

where K is a geometric factor associated to the Rosseland model. This analysis is repeated for $\Delta T = 1.0$ K over the model for a range temperature of $300.0 \leq T \leq 4000.0$ K, and an emissivity of $\epsilon = 0.85$ is used.

The temperature averaged values of the effective radiative conductivity for all nine matrix elements are presented in Table 4.2(a), where the calculated values imply an orthotropic behavior of the material (as the diagonal elements are about one order of magnitude greater than off-diagonal elements) and a symmetric behavior ($\kappa_{ij} = \kappa_{ji}$) which is in agreement with experimental data. Also, calculated temperature dependent conductivities are shown in Fig. 4.6, where the results are in good agreement with the Rosseland prediction. Therefore, the geometric factors associated to the best fit obtained from a cubic curve are extracted and presented in Table 4.2(b). From the matrix theory the effective radiative conductivity tensor possesses three mutually orthogonal principal axes (i.e. the orientation of the geometry where the off-diagonal terms are zero) which are associated with three real eigenvalues. These eigenvalues are listed in Table 4.2(c) and (d) regarding to panels (a) and (b), respectively. Comparison between the orthogonal values and the diagonal elements, which are different in magnitude, shows that the geometry was not well aligned with the chosen axes. As well, the through-the-thickness (TTT) direction (i.e. the smallest value κ_{yy}) is also less obvious when compared to the IP directions (κ_{xx} and κ_{zz}), which is a consequence of the fact that the material sample is small.

The values of the thermal conductivity calculated using the present method can be compared to the values provided by the manufacturer [86], as well as those available in the literature [88]. In these two references, the values in the TTT direction is presented. The TTT direction is defined as $\kappa_{ii} \ll \kappa_{jj}, \kappa_{kk}$, where $\kappa_{jj} \approx \kappa_{kk}$ is the IP direction. In the present work, the TTT direction corresponds to the y–axis. Since these results are obtained experimentally, they include all the physical phenomena that contribute to conductivity: the radiative conductivity, the gas phase conductivity

Table 4.2: (a) Temperature averaged effective radiative, (b) Geometric factor reconstructed from Rosseland model, (c) Temperature averaged effective radiative conductivity along the principal axis, and (d) Geometric factor reconstructed from Rosseland model along the principal axis.

(a)	$\langle\kappa\rangle_T$ [W/(m K)]			(b)	K [10^{-3} m]		
	x	***y***	***z***		***x***	***y***	***z***
x	1.767	0.176	0.111	***x***	2.072	0.207	0.130
y	0.176	1.301	0.372	***y***	0.207	1.526	0.436
z	0.111	0.372	1.583	***z***	0.130	0.436	1.856

(c)	$\langle\lambda\rangle_T$ [W/(m K)]			(d)	Λ [10^{-3} m]		
	1	**2**	**3**		**1**	**2**	**3**
	2.001	1.034	1.615		2.347	1.213	1.894

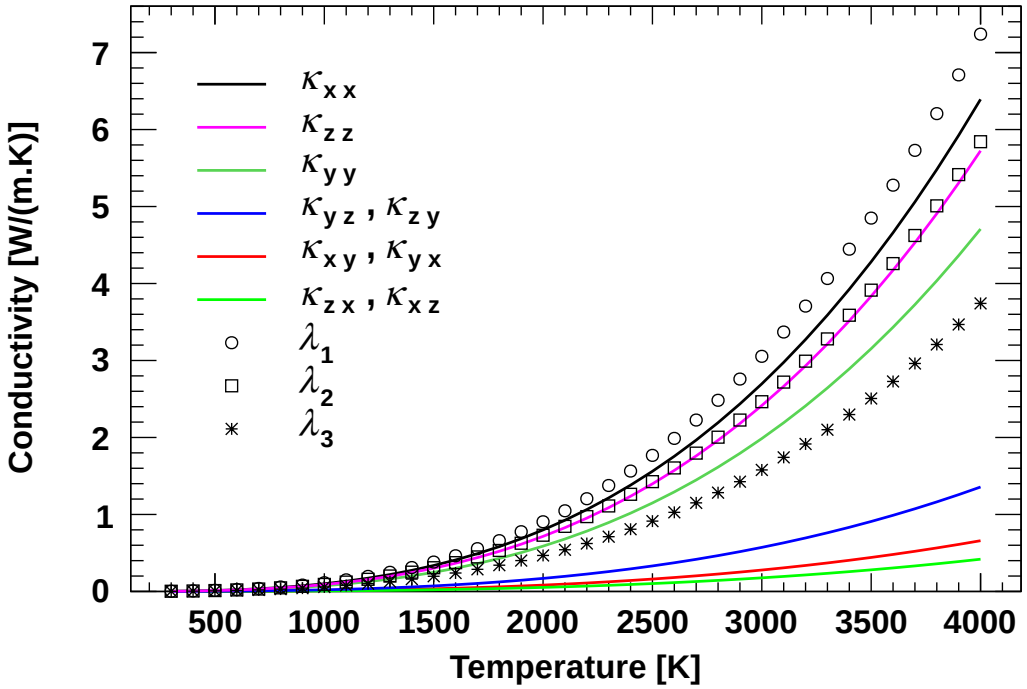

Figure 4.6: (Color online) Effective conductivity matrix elements as a function of temperature.

(argon), and the solid conductivity.

In order to properly compare the two values, the radiative conductivity calculated in this work is added to the solid conductivity value in the TTT direction calculated by Panerai et al. [31], so that $\kappa^{\text{eff}}_{TTT} = \kappa_{TTT} + \kappa^{\text{sol}}_{TTT}$. To calculate $\kappa^{\text{sol}}_{TTT}$, they use

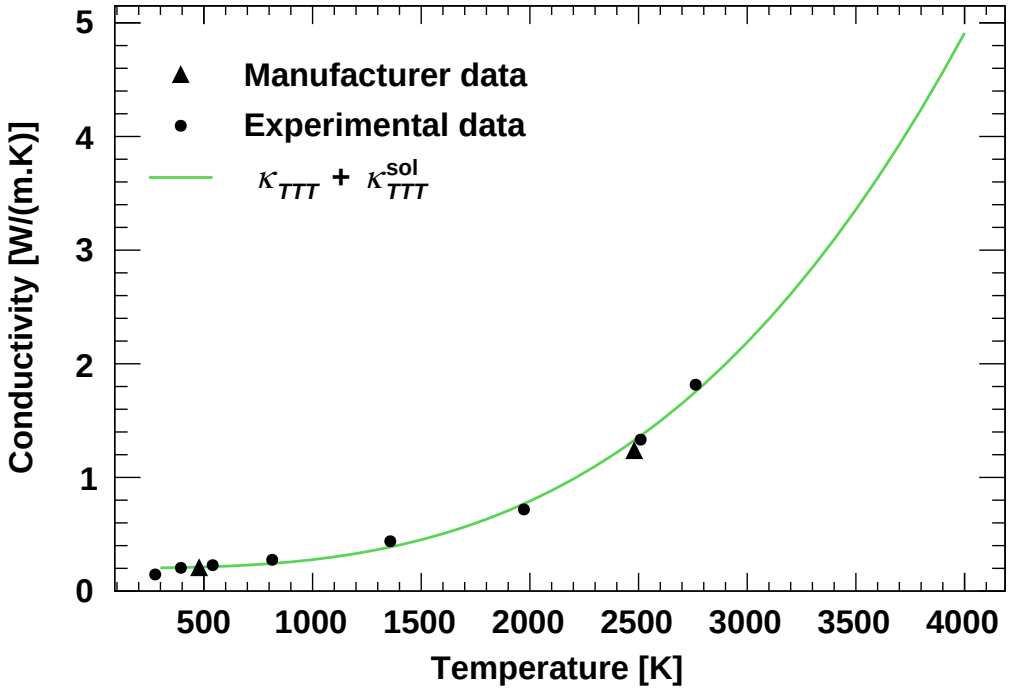

Figure 4.7: Comparison of the total effective conductivity with experimental results presented by Tran et al. [88] and Fiber Materials Inc. [86]. The total effective conductivity includes the radiative conductivity calculated in this work, and the solid conductivity $\kappa^{\text{sol}}_{TTT}$ calculated by Panerai et al. [31]

a 1 mm^3 cubic sample of FiberForm® in air, at 273 K. Even though it is expected that the solid conductivity slightly decreases with an increase in temperature [87], a constant value of $\kappa^{\text{sol}}_{TTT} = 0.203$ W/(m·K) is used here.

The comparison is presented in Fig. 4.7. As can be seen, the computed total effective conductivity $\kappa_{TTT} + \kappa^{\text{sol}}_{TTT}$ fits the experimental data remarkably well over the entire range of temperatures considered. Experimental data in the other directions are not readily available, but a factor of $\kappa_{IP}/\kappa_{TTT} = 2.4$ is mentioned in Tran et al. [88], and a factor of 2.0 in Weng and Martin [68]. Comparing to these ranges of values would also give a reasonable agreement for the κ_{xx} and κ_{zz} values calculated here.

Finally, it is important to point out that the temperature-dependent gas phase conductivity and radiative absorption are not accounted for in the present work. Moreover, the geometry of the sample used for the radiative conductivity, κ_{TTT}, is

different from the one used in Panerai et al. [31] to calculate $\kappa^{\text{sol}}_{TTT}$. Even though the axis with the minimum value is used for both components, the axes were likely oriented differently.

4.5 Remarks

The possibility of using X-ray micro-tomography for computing radiative conductivity was demonstrated. A robust algorithm to calculate the geometric configuration factors among the planar surface segments of FiberForm® using triangular mesh grids generated by micro-tomography was constructed. The calculated values highlighted the heterogeneous behavior of fibrous material. The net radiation exchange model and Fourier's law was used to investigate the radiation energy flux distribution within the FiberForm® micro-structure. The developed model accounts for both the angular and thermal dependence of the effective radiative conductivity. The extracted values of the effective radiative conductivity tensor elements manifested an orthotropic behavior of the material and the results also show that the cubic polynomials formulation of Rosseland model is valid in the studied case.

Chapter 5

Summary and future studies

5.1 Summary

The purpose of our study was to develop a model, based on the micro-structure characteristics, porosity, and surface emissivity values, to quantitatively analyze and determine the radiative properties of the carbon-based fibrous material as an insulation material used in TPS. More specifically, the effective radiative conductivity of the FiberForm® used in the TPSs of re-entry objects was evaluated using computer modeling.

A simplified three-dimensional DS model was developed which accounts for both the angular and thermal dependence of the effective radiative conductivity of a low-density fibrous material. Diffuse-gray (section 1.3.3 and section 2.7), net-radiation (section 2.8), and radiation heat conductivity (section 2.9) models were applied to analyze the radiative thermal transfer process. The basic equations were developed for analyzing radiative energy exchange within enclosures having black or diffuse-gray surfaces. The radiation energy exchange process among the enclosure diffuse-gray surfaces has been formulated via pre-calculated GCF's (chapter 2). An analytical expression was derived for the effective radiative conductivity as a function of direc-

tion and a wide range of temperature. The effective conductivity matrix elements as a function of direction and temperature were determined by applying a systematic temperature gradient procedure. The heterogeneous behavior of the FiberForm® was ultimately manifested.

The developed three-dimensional DS model was used for two different scenarios:

1. Using artificial geometry obtained from computer simulation,

2. Using realistic geometry obtained from tomography imaging.

First, an artificial geometry (section 3.2) with properties resembling those of FiberForm® was computationally constructed. The main goal of using this geometry was to validate the developed model to be applied into the second scenario. Using three-dimensional computed tomography imaging made it possible to apply the model into the true structure of FiberForm®. The artificial geometry was then substituted by three-dimensional X-ray micro-tomography imagery (chapter 4) to achieve a more realistic result.

As an important part of this thesis, a list of original contributions is outlined:

1. **A robust procedure to calculate the geometric configuration factor using discretized mesh surface area was proposed.**

   The calculation of the geometric configuration factor between finite surfaces requires the solution to a double area integral. Such integrals are exceedingly difficult to evaluate analytically except for very simple geometries. Even a numerical integration may often be problematic because of excessive CPU time requirements.

2. **The geometric properties of the discretized mesh surface area was used to accelerate the GCF calculation.**

Considerable effort has been directed toward tabulation and development of methods to suppress the CPU time requirement.

3. **The net-radiation method was combined to the radiation heat conductivity model to evaluate the radiative heat transfer process.**

   Radiative heat transfer rates within an enclosure without a participating medium has been developed by applying the geometric configuration factors calculated earlier.

4. **A systematic procedure was developed to determine the effective radiative conductivity matrix element.**

   The results from developed models are retained and implemented in a systematic radiative transient regime model to study the radiative conductivity properties of the FiberForm®.

5. **A C++ code was developed regarding the proposed model.**

   The studies developed in this work have been written based on a C++ manuscript. The data analysis part has been done using ROOT programing.

5.2 Future studies

The radiation-exchanged equations were developed in section 2.8 for an enclosure that does not contain an absorbing-scattering medium. The work in development at the time of writing this manuscript focuses on the effects of the presence of ambient gas on the radiative conductivity properties of the fibrous material. The attenuation of radiation is studied using Bouguer's law. As the radiation passes through a volume element $\mathrm{d}V$ of thickness $\mathrm{d}x$, its intensity q is reduced by absorption and scattering. For simplicity, the subscripts inc and out have been dropped. Intensity at some

distance in the media is expressed by Bouguer's law in differential form as

$$\mathrm{d}q = -\mu(x)\, q\, \mathrm{d}x\,. \tag{5.1}$$

When this equation is integrated, it becomes

$$q(x) = q(x_0)\, e^{-\int_{x_0}^{x} \mu(x)\, \mathrm{d}x}\,. \tag{5.2}$$

The attenuation coefficient (μ) describes the fraction of a beam (intensity) that is absorbed or scattered per unit thickness of the medium. More specifically, μ accounts for the number of atoms in a cubic cm volume of material and the probability of a photon being scattered or absorbed from the nucleus or an electron of one of these atoms. Attenuation coefficient μ [cm^{-1}] depends on the local properties of the medium (physical property). It is a function of temperature T, pressure P, concentration ρ and incident radiation wavelength λ.

Attenuation is composed of two volumetric coefficients, absorption μ_a and scattering μ_s. If the attenuation coefficient is a constant (i.e. a uniform density gas), Eq. (5.2) can be rewritten as

$$q(\Delta x) = q(x_0)\, e^{-(\mu_a+\mu_s)\,\Delta x}\,, \tag{5.3}$$

where $q(x_0)$ denotes the initial intensity leaving one of the surface segments within the fiducial volume (q_{out}) and $q(\Delta x)$ denotes the specific intensity (q_{inc}) after reaching another surface segment at a distance of Δx. Equations (4.11), (4.12) and (4.13) are rewritten as

$$q_{\text{out},i} - (1-\epsilon) \sum_{j=0}^{N-1} F_{ij} q_{\text{out},j}\, e^{-\mu_a\, \Delta x_{ij}} = \epsilon\sigma T_i^4, \quad i \in \{6, \ldots, N-1\}, \tag{5.4}$$

$$q_{\text{out},i} - \sum_{j=0}^{N-1} F_{ij} q_{\text{out},j}\, e^{-\mu_a\, \Delta x_{ij}} = 0, \qquad i \in \{0, 1, 2, 3, 4, 5\}, \tag{5.5}$$

$$q_{\text{inc},i} = \sum_{j=0}^{N-1} F_{ij}\, q_{\text{out},j}\, e^{-\mu_a\, \Delta x_{ij}}\,. \tag{5.6}$$

The attenuation coefficient values can sometimes be found in the literature, where attenuation data is mostly located in terms of the mass attenuation coefficient (a mass attenuation coefficient μ/ρ is converted to an attenuation coefficient μ if it is multiplied by the density ρ of the material). Mass attenuation coefficients for elements $Z = 1$ to 92, and for 48 compounds and mixtures of radiological interest are listed at the National Institute for Standards and Technology (NIST) [91]. The data on the NIST cover energies of photons (e.g. x-ray, gamma ray, bremsstrahlung) from 1 keV to 20 MeV.

The studies which have been done in this work were based on the assumption that the radiation process occurs in vacuum regimes. However, a more realistic model would be achieved if the vacuum space were filled with a participating medium that can absorb and scatter radiation. The model developed in this study, adding ambient gas, can be used to manifest the effects of the presence of ambient gas on the radiative conductivity properties of the fibrous material.

Bibliography

[1] N. Nouri, A. Martin, Three dimensional radiative heat transfer model for the evaluation of the anisotropic effective conductivity of fibrous materials, International Journal of Heat and Mass Transfer 83 (2015) 629–635. doi:10.1016/j.ijheatmasstransfer.2014.12.041.

[2] http://www.nasa.gov/.

[3] Cooper, Th D., and O. O. Srp., Refractory Metals and Their Protection. Aerospace Eng. 22.1 (1963).

[4] Krier, Carol Alnoth. Coatings for the protection of refractory metals from oxidation. No. DMIC-162. BATTELLE MEMORIAL INST COLUMBUS OH DEFENSE METALS INFORMATION CENTER, 1961.

[5] Samsonov, Grigorii Valentinovich, and Aleksej P. Epik. Coatings of high-temperature materials. Springer US, 1966.

[6] Wurst, J. C., et al. high temperature evaluation of aerospace materials, 1966.

[7] Priceman, Gs., Development of Fused Slurry Silicide Coatings for the Elevated-Temperature Oxidation Protection of Columbium and Tantalum Alloys. (1968).

[8] Remake, W. G., Latve, J. D. refractory ceramic and intermetallic compounds, aerospace engineering, (1963)

[9] Strauss, Eric L., The Application of Resin-Impregnated Porous Ceramics to Re-Entry Vehicle Heat Shields. Proceedings: Sponsored Jointly by the Air Force Office of Scientific Research and Arthur D. Little, Inc (1962): 7.

[10] Sunday, Terry L., and John R. London. The X-20 space plane: Past innovation, future vision. Acta Astronautica 21.4 (1990): 223-242.

[11] Hurwicz, Henryk, and Robert Mascola. Thermal protection systems. application research of materials properties and structural concepts, (1965).

[12] Shields, S. Investigation of Insulative Heat Shield Attachment Systems. Research and Technology Division, Wright-Patterson Air Force Base, Ohio, AFFDL-TR-65-55 (April 1965) (1965).

[13] Davis, R. M., and J. W. McCown. Radiative vs ablative heat shield concepts for manned lifting entry vehicles. Journal of Spacecraft and Rockets 4.6 (1967): 725-731.

[14] Vafai, Kambiz, and Lu Zhu. Two-layered micro channel heat sink, devices and systems incorporating same. U.S. Patent No. 6,457,515. 1 Oct. 2002.

[15] Wang, Chien-Chang, Chen-I. Hung, and Wei-Hsin Chen. Design of heat sink for improving the performance of thermoelectric generator using two-stage optimization. Energy 39.1 (2012): 236-245.

[16] Lorenz, G. C., and L. W. Woodruff. Hypersonic turbulent transpiration cooling including downstream effects. AIAA Journal 4.6 (1966): 969-975.

[17] Leadon, Bernard M. The status of heat transfer control by mass transfer for permanent surface structures. Aerodynamically Heated Structures (1962): 171.

[18] Auslander, D. M. , D. B. Spaulding, and T. R. Sundaram. The calculation of heat and mass transfer through the turbulent boundary layer on a flat plate at

high mach numbers, with and without chemical reaction(Heat and mass transfer through turbulent boundary layer on flat plate at high mach numbers with and without chemical reaction). 1964. (1964): 211-276.

[19] Transpirationally cooled heat ablation system. U.S. Patent 3,321,154, issued May 23, 1967.

[20] Vaniman, J., et al. Ablative thermal protection systems. NASA STI/Recon Technical Report A 83 (1983): 42257.

[21] McConarty, W. A., and F. M. Anthony. Design and Evaluation of Active Cooling Systems for Mach 6 Cruise Vehicle Wings. Work 7305 (1971): 901001.

[22] Fiber Materials, Inc.: LCA Final Report. FMI Contract NAS2-13982 deliverable, July 1994.

[23] R. A. S. Beck, D. M. Driver, M. J. Wright, H. H. Hwang, K. T. Edquist, S. A. Sepka, Development of the mars science laboratory heatshield thermal protection system, Journal of Spacecraft and Rockets 51 (4) (2014) 1139–1150. doi:10.2514/1.A32635.

[24] Seeing red, Nature 479 (7374) (2011) 446–446. doi:10.1038/479446a.

[25] D. Bose, T. White, M. Mahzari, K. Edquist, Reconstruction of aerothermal environment and heat shield response of mars science laboratory, Journal of Spacecraft and Rockets 51 (4) (2014) 1174–1184. doi:10.2514/1.A32783.

[26] K. A. Trumble, I. Cozmuta, A. S. Sepka, P. Jenniskens, M. Winter, Postflight aerothermal analysis of the stardust sample return capsule, Journal of Spacecraft and Rockets 47 (5) (2010) 765–774. doi:10.2514/1.41514.

[27] A. Martin, I. D. Boyd, Modeling of heat transfer attenuation by ablative gases during the stardust re-entry, Journal of Thermophysics and Heat TransferIn Revision (Manuscript 2013-06-T4202). doi:10.2514/3.T4202.

[28] A. Martin, I. D. Boyd, Modeling of heat transfer attenuation by ablative gases during stardust re-entry, in: 50th AIAA Aerospace Sciences Meeting, AIAA Paper 2012-0814, Nashville, TN, 2012. doi:10.2514/6.2012-814.

[29] Y.-K. Chen, F. S. Milos, Ablation and thermal response program for spacecraft heatshield analysis, Journal of Spacecraft and Rockets 36 (3) (1999) 475–483. doi:10.2514/2.3469.

[30] C. Szalai, E. Slimko, P. Hoffman, Mars science laboratory heatshield development, implementation, and lessons learned, Journal of Spacecraft and Rockets 51 (4) (2014) 1167–1173. doi:10.2514/1.A32673.

[31] F. Panerai, J. C. Ferguson, J. R. Lachaud, A. Martin, M. J. Gasch, N. N. Mansour, Analysis of carbon fiber felts for flexible ablators using synchrotron hard x-ray micro-tomography, in: 8th European Symposium on Aerothermodynamics for Space Vehicles, no. 89747, Lisbon, Portugal, 2015. doi:10.13140/RG.2.1.2661.0084.
URL http://www.congrexprojects.com/Custom/15A01/Papers/Room%201.1/Tuesday/Measurement%20techniques%20I/89747_Panerai.pdf

[32] Tran, Huy K. Development of Light Weight Ceramic Ablators and Arc-jet Test Results. National Aeronautics and Space Administration, Ames Research Center, 1994.

[33] Chandrasekhar, Subrahmanyan. Radiative transfer. Courier Corporation, 2013.

[34] T. W. Tong, C. L. Tien, Radiative heat transfer in fibrous insulations – part i: Analytical study, Journal of Heat Transfer 105 (1) (1983) 70–75. doi:10.1115/1.3245561.

[35] T. W. Tong, Q. S. Yang, C. L. Tien, Radiative heat transfer in fibrous insulations – part ii: Experimental study, Journal of Heat Transfer 105 (1) (1983) 76–81. doi:10.1115/1.3245562.

[36] K. Wang, C. Tien, Radiative heat transfer through opacified fibers and powders, Journal of Quantitative Spectroscopy and Radiative Transfer 30 (3) (1983) 213–223. doi:10.1016/0022-4073(83)90059-6.

[37] R. L. Houston, S. A. Korpela, Heat transfer through fiberglass insulation, in: Proceedings of the 7th International Heat Transfer Conference, Vol. 2, 1982, pp. 499–504.

[38] R. P. Banas, G. R. Cunnington, Determination of effective thermal conductivity for the space shuttle orbiter's reusable surface insulation (rsi), in: Thermophysics and Heat Transfer Conference, AIAA Paper 1974-730, 1974. doi:10.2514/6.1974-730.

[39] J. Lachaud, I. Cozmuta, N. N. Mansour, Multiscale approach to ablation modeling of phenolic impregnated carbon ablators, Journal of Spacecraft and Rockets 47 (6) (2010) 910–921. doi:10.2514/1.42681.

[40] F. S. Milos, Y.-K. Chen, T. Gökçen, Nonequilibrium ablation of phenolic impregnated carbon ablator, Journal of Spacecraft and Rockets 49 (5) (2012) 894–904. doi:10.2514/1.A32298.

[41] Verschoor, J. D., and Paul Greebler. Heat transfer by gas conduction and radiation in fibrous insulation. (1952): 961-968.

[42] Bankvall, Claes G. Heat transfer in fibrous materials. National Swedish Institute for Building Research, 1972.

[43] Pelanne, Charles M. Heat flow principles in thermal insulations. Journal of Building Physics 1.1 (1977): 48-80.

[44] Burns, P. J., and C. L. Tien. Natural convection in porous media bounded by concentric spheres and horizontal cylinders. International Journal of Heat and Mass Transfer 22.6 (1979): 929-939.

[45] Tong, T. W., and C. L. Tien. Analytical models for thermal radiation in fibrous insulations. Journal of Building Physics 4.1 (1980): 27-44.

[46] Rowley, F. B., et al. Gas is an important factor in the thermal conductivity of most insulating materials, Part I. ASHVE J. Sect. Heating, Piping Air-cond (1951): 103-109.

[47] Preisendorfer, Rudolph W. Radiative Transfer on Discrete Spaces: International Series of Monographs in Pure and Applied Mathematics. Vol. 74. Elsevier, 2014.

[48] Viskanta, Raymond, and M. P. Menguc. Radiation heat transfer in combustion systems. Progress in Energy and Combustion Science 13.2 (1987): 97-160.

[49] Viskanta, R., and M. P. Menguc. Radiative transfer in dispersed media. Applied Mechanics Reviews 42.9 (1989): 241-259.

[50] Modest MF. Radiative heat transfer. New York: McGraw-Hill, 1993.

[51] Van der Held, E. F. M. The contribution of radiation to the conduction of heat. Applied Scientific Research, Section A 3.3 (1952): 237-249.

[52] Hager Jr, Nathaniel E., and Robin C. Steere. Radiant heat transfer in fibrous thermal insulation. Journal of Applied Physics 38.12 (1967): 4663-4668.

[53] Strong, H. M., F. P. Bundy, and H. P. Bovenkerk. Flat panel vacuum thermal insulation. Journal of Applied Physics 31.1 (1960): 39-50.

[54] Larkin, Bert K., and Stuart W. Churchill. Heat transfer by radiation through porous insulations. AIChE Journal 5.4 (1959): 467-474.

[55] Aronson, James R., et al. Infrared emittance of fibrous materials. Applied optics 18.15 (1979): 2622-2633.

[56] V. A. Petrov, Combined radiation and conduction heat transfer in high temperature fiber thermal insulation, International Journal of Heat and Mass Transfer 40 (9) (1997) 2241–2247. doi:10.1016/S0017-9310(96)00242-6.

[57] Kowalski, G. J., and J. W. Mitchell. An analytical and experimental investigation of the heat transfer mechanisms within fibrous media. American Society of Mechanical Engineers 1 (1979).

[58] S. C. Lee, Radiation heat transfer model for fibers oriented parallel to diffuse boundaries, Journal of Thermophysics and Heat Transfer 2 (4). doi:10.2514/3.104.

[59] H. T. T. Kamdem, D. D. Baillis, Reduced models for radiative heat transfer analysis through anisotropic fibrous medium, Journal of Heat Transfer 132 (2010) 072703–1 – 072703–8. doi:10.1115/1.4000994.

[60] Tien, Chang-Lin, and B. L. Drolen. Thermal radiation in particulate media with dependent and independent scatering. Annual Review of Heat Transfer 1.1 (1987).

[61] R. Siegel, J. R. Howell, M. P. Menguç, Thermal radiation heat transfer, 5th Edition, CRC Press, 2012.

[62] Lee, S. C. Effect of fiber orientation on thermal radiation in fibrous media. International journal of heat and mass transfer 32.2 (1989): 311-319.

[63] A. van Eekelen, J. R. Lachaud, Numerical validation of an effective radiation heat transfer model for fiber preforms, Journal of Spacecraft and Rockets 48 (3) (2011) 534–537. doi:10.2514/1.51865.

[64] N. N. Mansour, F. Panerai, A. Martin, D. Y. Parkinson, A. MacDowell, A. Haboub, T. A. Sandstrom, T. Fast, G. L. Vignoles, J. Lachaud, A new approach to light-weight ablators analysis: From micro-tomography measurements to statical analysis and modeling, in: 44th AIAA Thermophysics Conference, AIAA Paper 2013-2768, San Diego, CA, 2013, pp. 1–11. doi:10.2514/6.2013-2768.

[65] Mendes, Miguel AA, et al. Experimental validation of simplified conductionradiation models for evaluation of Effective Thermal Conductivity of open-cell metal foams at high temperatures. International Journal of Heat and Mass Transfer 78 (2014): 112-120.

[66] J. Marschall, M. E. Cox, Gas permeability of lightweight ceramic ablators, Journal of Thermophysics and Heat Transfer 13 (3) (1999) 382–384. doi:10.2514/2.6451.

[67] J. Marschall, F. S. Milos, Gas permeability of rigid fibrous refractory insulations, Journal of Thermophysics and Heat Transfer 12 (4) (1998) 528–535. doi:10.2514/2.6372.

[68] H. Weng, A. Martin, Numerical investigation of pyrolysis gas blowing pattern and thermal response using orthotropic charring ablative material, Journal of Thermophysics and Heat TransferIn Press (Control ID 2014-09-T4576). doi:10.2514/1.T4576.

[69] H. Weng, A. Martin, Numerical investigation of pyrolysis gas blowing pattern and thermal response using orthotropic charring ablative material, in: 11th AIAA/ASME Joint Thermophysics and Heat Transfer Conference, AIAA Paper 2014-2121, Atlanta, GA, 2014. doi:10.2514/6.2014-2121.

[70] Grujicic, M., et al. Heat transfer and effective thermal conductivity analyses in carbon-based foams for use in thermal protection systems. Proceedings of the Institution of Mechanical Engineers, Part L: Journal of Materials Design and Applications 219.4 (2005): 217-230.

[71] Morgan, D. R. Coal based carbon foam for high temperature applications. MS Thesis, University of North Texas, Denton, Texas, 2001.

[72] Rushmeier, Holly E., Daniel R. Baum, and David E. Hall. Accelerating the hemicube algorithm for calculating radiation form factors. Journal of heat transfer 113.4 (1991): 1044-1047.

[73] Campbell III, Alvin T., and Donald S. Fussell. Adaptive mesh generation for global diffuse illumination. ACM SIGGRAPH Computer Graphics. Vol. 24. No. 4. ACM, 1990.

[74] Howell, John R. A catalog of radiation configuration factors. McGraw-Hill Book Company, 1982.

[75] Kurosaki, Yasuo, and Jun Yamada. Radiation Transport in Porous or Fibrous Media. Convective Heat and Mass Transfer in Porous Media. Springer Netherlands, 1991. 347-390.

[76] Lander, R. M. Gas is an important factor in the thermal conductivity of most insulating materials, Part II. ASHVE J. Sect. Heating, Piping Air-cond (1954): 121-126.

[77] H. K. Tran, C. E. Johnson, D. J. Rasky, F. C. L. Hui, M.-T. Hsu, Y. K. Chen, Phenolic impregnated carbon ablators (pica) for discovery class missions, in: 31st AIAA Thermophysics Conference, AIAA Paper 1996-1911, New Orleans, LA, 1996, pp. 1–14. doi:10.2514/6.1996-1911.

[78] D. Eberly, Intersection of cylinders, Tech. rep., Geometric Tools, LLC (2010).

[79] A. Ameri, J. D. Felske, Radiation configuration factors for obliquely oriented finite length circular cylinders, International Journal of Heat and Mass Transfer 25 (5) (1982) 728–736. doi:10.1016/0017-9310(82)90180-6.

[80] E. Sparrow, A new and simpler formulation for radiative angle factors, Journal of Heat Transfer 85 (2) (1963) 81–88. doi:10.1115/1.3686058.

[81] F. S. Milos, Y.-K. Chen, Ablation and thermal response property model validation for phenolic impregnated carbon ablator, Journal of Spacecraft and Rockets 47 (5). doi:10.2514/1.42949.

[82] A. Martin, I. D. Boyd, I. Cozmuta, M. J. Wright, Kinetic rates for gas phase chemistry of phenolic based carbon ablator decomposition in atmospheric air, Journal of Thermophysics and Heat TransferIn Press (Manuscript 2013-05-T4184.R2). doi:10.2514/3.T4184.

[83] A. Martin, I. D. Boyd, I. Cozmuta, M. J. Wright, Chemistry model for ablating carbon-phenolic material during atmospheric re-entry, in: 48th AIAA Aerospace Sciences Meeting and Exhibit, AIAA Paper 2010-1175, Orlando, FL, 2010. doi:10.2514/6.2010-1175.

[84] H. Weng, A. Martin, Multidimensional modeling of pyrolysis gas transport inside charring ablative materials, Journal of Thermophysics and Heat Transfer 28 (4) (2014) 583–597. doi:10.2514/1.T4434.

[85] H. Weng, S. C. C. Bailey, A. Martin, Numerical study of geometrical effects on charring ablative arc-jet samples, International Journal of Heat and Mass Transfer 80 (2015) 570–596. doi:10.1016/j.ijheatmasstransfer.2014.09.040.

[86] Fiber Materials Inc. Fiberform® rigid insulation [online] (2014). Retrieved from http://www.fibermaterialsinc.com/product/fiberform-rigid-insulation/ [cited 04/23/2015].

[87] Entegris, Inc., Properties and characteristics of graphite – for the semiconductor insdustry, Tech. Rep. 6205-7329CRE-0513, Entegris, Inc. (May 2013).

[88] H. K. Tran, C. E. Johnson, D. J. Rasky, F. Hui, M. Hsu, T. Chen, Y. Chen, D. Paragas, L.Kobayashi, Phenolic impregnated carbon ablators (pica) as thermal protection systems for discovery missions, Technical Report NASA-TM-110440, NASA Ames Research Center, Moffett Field, CA (April 1997).

[89] Lawrence Berkeley National Laboratory http://www.lbl.gov/.

[90] University of Kentucky High Performance Computing http://www.uky.edu/ukat/hpc.

[91] National Institute for Standards and Technology http://www.nist.gov/pml/data/xraycoef/index.cfm.

Copyright© Nima Nouri, 2015.

Vita

Nima Nouri earned his B.Sc. in Atomic and Molecular Physics from Qom University, Iran, in 2006. He continued his studies as a M.Sc. student in Photonics at the Laser and Plasma Research Institute, S. Beheshti University, Iran, receiving his degree in 2009. His research was focused on computational studies of nano-pulse laser ablation processes in Laser Induced Breakdown Spectroscopy (LIBS). After completing this studies in Iran, he enrolled at the University of Kentucky as a Ph.D. student in the Physics and Astronomy department in 2011. His Ph.D. research under Prof. Bradley Plaster focused on the development of general computational and numerical techniques for nuclear and particle physics experiments, especially in experiments probing the fundamental symmetries of the early universe. Simultaneously, he pursued a M.Sc. in the Mechanical Engineering department at the University of Kentucky with Prof. Alexandre Martin. His M.Sc. research focused on the development of computational and numerical methods for the study of the Thermal Protection Systems (TPS) employed in reentry vehicles.

Papers in Refereed Journals

1. **Nima Nouri**, Francesco Panerai, Nagi N. Mansour, Alexandre Martin, "Radiative heat transfer analysis for the evaluation of the anisotropic effective conductivity of a low-density fibrous carbon material using X-ray micro-tomography", International Journal of Heat and Mass Transfer (in review).

2. **Nima Nouri**, Alexandre Martin, "Three dimensional radiative heat transfer model for the evaluation of the anisotropic effective conductivity of fibrous materials", International Journal of Heat and Mass Transfer **8**3, 629 (2015).

Papers in Refereed Conference Proceedings

1. **Nima Nouri**, Alexandre Martin, "Gas-phase radiative absorption inside a low-density fibrous carbon material", AIAA Science and Technology, San Diego, California 2016 (accepted).